UC San Diego
UC San Diego Previously Published Works

Title

The Simons Observatory: Cryogenic half wave plate rotation mechanism for the small aperture telescopes

Permalink

Journal

ISSN

Authors

Yamada, K
Bixler, B
Sakurai, Y
et al.

Publication Date

DOI

Copyright Information

Peer reviewed

RESEARCH ARTICLE | FEBRUARY 22 2024

The Simons Observatory: Cryogenic half wave plate rotation mechanism for the small aperture telescopes

K. Yamada ✉ iD ; B. Bixler iD ; Y. Sakurai ✉ iD ; P. C. Ashton iD ; J. Sugiyama iD ; K. Arnold iD ; J. Begin iD ;
L. Corbett iD ; S. Day-Weiss iD ; N. Galitzki iD ; C. A. Hill iD ; B. R. Johnson iD ; B. Jost iD ; A. Kusaka iD ;
B. J. Koopman iD ; J. Lashner iD ; A. T. Lee iD ; A. Mangu iD ; H. Nishino iD ; L. A. Page iD ; M. J. Randall iD ;
D. Sasaki iD ; X. Song iD ; J. Spisak iD ; T. Tsan iD ; Y. Wang iD ; P. A. Williams iD

Check for updates

View Online   Export Citation   CrossMark

The Simons Observatory: Cryogenic half wave plate rotation mechanism for the small aperture telescopes

View Online   Export Citation   CrossMark

K. Yamada,[1,a] [ID]   B. Bixler,[2] [ID]   Y. Sakurai,[3,4,a] [ID]   P. C. Ashton,[4,5,6,b] [ID]   J. Sugiyama,[1] [ID]   K. Arnold,[2] [ID]
J. Begin,[7] [ID]   L. Corbett,[5,6] [ID]   S. Day-Weiss,[7] [ID]   N. Galitzki,[8,9] [ID]   C. A. Hill,[5,6] [ID]   B. R. Johnson,[10] [ID]
B. Jost,[4] [ID]   A. Kusaka,[1,4,5,11] [ID]   B. J. Koopman,[12] [ID]   J. Lashner,[12] [ID]   A. T. Lee,[5,6] [ID]   A. Mangu,[6] [ID]
H. Nishino,[11] [ID]   L. A. Page,[7] [ID]   M. J. Randall,[2] [ID]   D. Sasaki,[1] [ID]   X. Song,[6] [ID]   J. Spisak,[2] [ID]
T. Tsan,[2] [ID]   Y. Wang,[7] [ID]   and   P. A. Williams[5] [ID]

AFFILIATIONS

[1] Department of Physics, Graduate School of Science, The University of Tokyo, Tokyo 113-0033, Japan
[2] Department of Physics, University of California, San Diego, La Jolla, California 92093, USA
[3] Graduate School of Natural Science and Technology, Okayama University, Okayama 700-8530, Japan
[4] Kavli Institute for the Physics and Mathematics of the Universe (WPI), UTIAS, The University of Tokyo, Chiba 277-8583, Japan
[5] Physics Division, Lawrence Berkeley National Laboratory, Berkeley, California 94720, USA
[6] Department of Physics, University of California, Berkeley, California 94720, USA
[7] Joseph Henry Laboratories of Physics, Jadwin Hall, Princeton University, Princeton, New Jersey 08544, USA
[8] Department of Physics, University of Texas at Austin, Austin, Texas 78722, USA
[9] Weinberg Institute for Theoretical Physics, Texas Center for Cosmology and Astroparticle Physics, Austin, Texas 78712, USA
[10] Department of Astronomy, University of Virginia, Charlottesville, Virginia 22904, USA
[11] Research Center for the Early Universe, School of Science, The University of Tokyo, Tokyo 113-0033, Japan
[12] Wright Laboratory, Department of Physics, Yale University, New Haven, Connecticut 06520, USA

[a] Authors to whom correspondence should be addressed: ykyohei@cmb.phys.s.u-tokyo.ac.jp; yuki.sakurai727@gmail.com;
and ysakurai@s.okayama-u.ac.jp
[b] Current address: Advanced Technology and Systems Division, SRI International, Menlo Park, CA 94025, USA.

ABSTRACT

We present the requirements, design, and evaluation of the cryogenic continuously rotating half-wave plate (CHWP) for the Simons Observatory (SO). SO is a cosmic microwave background polarization experiment at Parque Astronómico de Atacama in northern Chile that covers a wide range of angular scales using both small (∅0.42 m) and large (∅6 m) aperture telescopes. In particular, the small aperture telescopes (SATs) focus on large angular scales for primordial B-mode polarization. To this end, the SATs employ a CHWP to modulate the polarization of the incident light at 8 Hz, suppressing atmospheric $1/f$ noise and mitigating systematic uncertainties that would otherwise arise due to the differential response of detectors sensitive to orthogonal polarizations. The CHWP consists of a 505 mm diameter achromatic sapphire HWP and a cryogenic rotation mechanism, both of which are cooled down to ~50 K to reduce detector thermal loading. Under normal operation, the HWP is suspended by a superconducting magnetic bearing and rotates with a constant 2 Hz frequency, controlled by an electromagnetic synchronous motor. We find that the number of superconductors and the number of magnets that make up the superconducting magnetic bearing are important design parameters, especially for the rotation mechanism's vibration performance. The rotation angle is detected through an angular encoder with a noise level of 0.07 μrad $\sqrt{s}$. During a cooldown process, the rotor is held in place by a grip-and-release mechanism that serves as both an alignment device and

27 February 2024 19:16:45

a thermal path. In this paper, we provide an overview of the SO SAT CHWP: its requirements, hardware design, and laboratory performance.

I. INTRODUCTION

The cosmic microwave background (CMB) radiation is the oldest detectable light in the universe, originating from the epoch of recombination. Its polarization is dominated by parity-even "E-mode" patterns, primarily sourced by density fluctuations in the early universe.[1,2] Primordial tensor perturbations are predicted to produce parity-odd "B-mode" polarization with an angular spectrum peaking at degree scales.[3,4] The rapid expansion of the early universe, called inflation, could produce tensor perturbations.[5–7]

A measurement of the primordial B-mode polarization signature would constrain models of the early universe and contribute to the understanding of physics at grand unified theory (GUT) energy scales.[8] The primordial B-mode signal is subdominant to both E-modes and several foreground sources, including polarized galactic emission, mainly from synchrotron and thermal dust,[9,10] and E- to B-mode conversion through gravitational lensing.[11] Separating primordial B-mode polarization from galactic foregrounds requires a wide frequency coverage, while efficient lensing B-mode separation requires a high resolution and large sky coverage.[12–14]

The Simons Observatory (SO) is a CMB experiment located at Cerro Toco (5200 m) in the Chilean Atacama Desert.[15,16] The nominal observatory consists of three small aperture telescopes (SATs), each with an aperture of 42 cm targeting large angular scales,[17,18] and one large aperture telescope (LAT), with an aperture of 6 m targeting arcminute angular scales.[19–21] The combined arrays of the SATs and the LAT employ over 60 000 transition-edge sensor (TES) bolometers.[22–24] The SATs are designed for the primary science goal of constraining primordial B-modes and, therefore, probe a sufficiently wide range of frequency bands and angular scales. In order to address these requirements, each SAT is sensitive to large angular scales of $30 < \ell < 300$ with 10% fractional sky coverage and has two primary frequency bands with bandwidths ranging from about 20% to 45% of the central frequencies.[25] Two SATs cover middle frequencies (MFs), with band centers at 93 and 145 GHz, while the third SAT covers ultra-high frequencies (UHFs), centering at 225 and 280 GHz.

Various modulation techniques have been used in CMB polarization experiments.[26–37] The rapid modulation of incident polarization by a half-wave plate (HWP) is one of the most promising techniques to separate the large scale CMB B-mode polarization signal from large unpolarized atmospheric $1/f$ noise, while using an instrument with a large optical throughput and a large number of multi-chroic pixels.[38–44]

The SO SATs employ a cryogenic continuously rotating half-wave plate (CHWP) polarization modulator to achieve sensitive observations at large angular scales. In this paper, we describe the requirements, design, and evaluation test results of the SO SAT CHWP rotation mechanism for the MF and UHF bands. The development and study of low frequencies (LFs), having center band

frequencies of 27 and 39 GHz, are under way and will be reported elsewhere. Section II provides an overview of the basic functionality of the polarization modulator, Sec. III presents the requirements, Sec. IV presents the design of subsystems, Sec. V presents the results of laboratory performance, and Sec. VI summarizes the development and describes future prospects.

II. HALF-WAVE PLATE POLARIMETRY

Observing primordial B-modes requires nK sensitivity, especially at degree angular scales. The challenge for ground-based polarimeters is to characterize faint signals in the presence of comparably large-amplitude unpolarized atmospheric fluctuations, in addition to polarized emission from the atmosphere,[46,47] the ground, and the instrument itself. While atmospheric noise is mitigated by the high altitude and low water vapor of the SO site, it is, nevertheless, difficult to control this contamination due to spatial and temporal fluctuations caused by local weather conditions. The atmospheric noise enters the detector time ordered data (TOD) as $1/f$ noise, reducing sensitivity at large angular scales.[48–51]

Experiments without rapid polarization usually mitigate the atmospheric $1/f$ noise and reconstruct the linear polarization by differencing detectors with orthogonal antennas.[52–54] However, any mismatched response between orthogonal detectors leads to intensity-to-polarization (I-to-P) leakage, which contaminates the cosmological polarization signal.[55]

In order to mitigate both $1/f$ noise and I-to-P leakage, the SATs employ a CHWP-based polarization modulation system, a commonly used technique among millimeter and sub-millimeter polarimeters. The HWP consists of a birefringent material that introduces a phase difference of 180° between the ordinary and extraordinary axes. While passing through the HWP, the incident polarization rotates twice the angle between its vector and the HWP extraordinary axis. If the HWP is continuously rotating, the measured linear polarization signal rotates synchronously and is modulated above $1/f$ noise fluctuations by setting the appropriate rotation frequency. The HWP modulated signal incident on a polarimeter sensitive to a single linear polarization is expressed as

$$d_m(t) = I(t) + \varepsilon \mathrm{Re}[(Q(t) + iU(t))m(\chi)], \qquad (1)$$

where t is time; I, Q, and U are the Stokes vectors of the incident light, assuming $V = 0$; ε is the HWP polarization modulation efficiency; $\chi(t)$ is the rotation angle of the HWP; and

$$m(\chi) = \exp(-i4\chi) \qquad (2)$$

is the modulation function. To extract the intensity signal, we low-pass-filter the modulated data. To extract the linear polarization signals, Q and U, we band-pass-filter the modulated data around
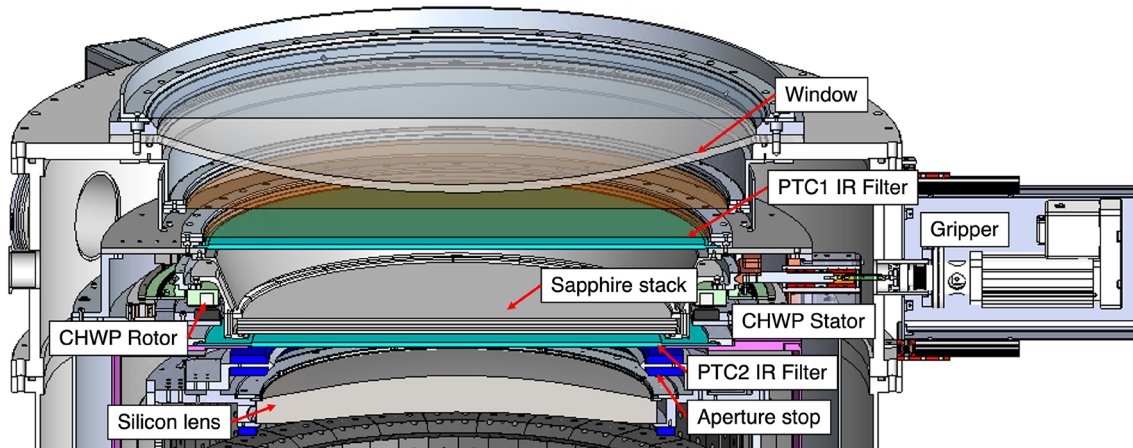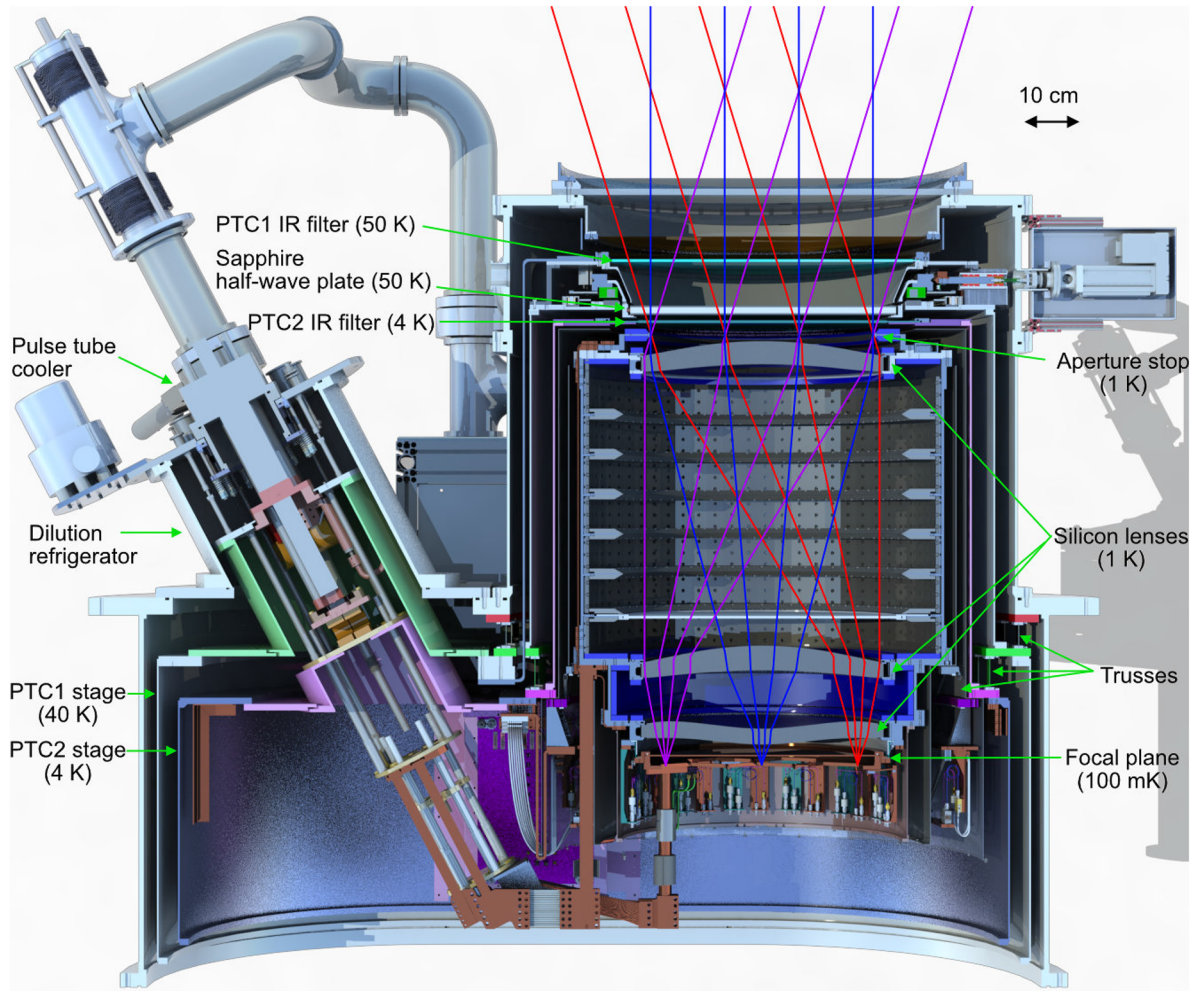
FIG. 1. Computer-aided design (CAD) cross section of the small-aperture telescope's receiver.[19] The superposed optical ray traces[45] are approximations and for illustrative purposes only. The SAT receiver employs an outer vacuum shell and two thermal shells cooled by two pulse tube coolers (PTCs). We refer to the two thermal shells as the PTC1 stage and the PTC2 stage. The CHWP rotation mechanism and PTC1 infrared (IR) blocking alumina filter are located on the PTC1 stage, and the PTC2 IR blocking alumina filter is located on the PTC2 stage. The temperatures shown for each component are nominal values.

the modulation frequency, multiply by the complex conjugate of the modulation function, $m(\chi)$, and apply a low-pass filter to it. We call this procedure demodulation.[41] There is no need for differencing pairs of orthogonal detectors in demodulation, and thus, all functional TESs in the array can operate independently.

The CHWP employs a Pancharatnam-style[56] achromatic HWP (AHWP) composed of three single-crystal sapphire plates. Sapphire was chosen because it has high thermal conductivity and low millimeter-wave absorption. The AHWP allows for coverage of a wide frequency band, and it has been employed in several previous CMB experiments[34,38,44,57,58] as well as included in the design of planned instruments.[59] The design of the AHWP is similar to that used in the Simons Array experiment, including the three slabs of sapphire with anti-reflection (AR) coating.[42] The control of systematic effects from the AHWP is a crucial aspect of HWP polarimetry.[58,60,61] The study of detailed performance and systematics of the SO AHWP is reported by Sugiyama *et al.*[62] The design of the rotation mechanism inherits many aspects of the analogous system in the Simons Array experiment.[44] However, the details of the implementation have been modified according to the unique requirements of the SO SAT receiver, as shown in Fig. 1.

The driving philosophy behind the CHWP system design is to ensure stability, both mechanically and thermally. Since the CHWP is located in the SAT's main beam (Fig. 1), any unpredictable behavior carries a risk of contaminating the polarization signal from the sky.[45] Therefore, we require any variation in the CHWP system other than its fast modulation to be small, slowly varying, and measurable where possible. Furthermore, we look for robust design solutions that will withstand years of continuous operation at the Simons Observatory site while minimizing maintenance and telescope downtime. Finally, we develop the CHWP rotation mechanism as a modular system that can be tested with more frequent iterations before being integrated with the complete SAT cryostat. The SAT receiver employs an outer vacuum shell and two thermal shells cooled by two pulse tube coolers (PTCs).[63] We refer to the two thermal shells as the PTC1 stage and the PTC2 stage with nominal temperatures of 40 and 4 K, respectively. The CHWP mechanism is mounted on the most skyward flange of the PTC1 stage (Fig. 1).

III. REQUIREMENTS

Table I summarizes the CHWP requirements and achieved values. The system design relies on the heritage of the CHWP for the Simons Array telescopes,[44] and the requirements qualitatively remain the same. Notable differences to the requirements include: (a) a larger optical throughput requiring an optical diameter of 490 mm and the placement of the HWP optics close to the telescope's aperture stop, (b) relaxed requirements on the physical volume available to the system, and (c) a larger variation in the gravity vector due to the addition of bore sight rotation about the SAT's optical axis to the scan strategy, resulting in the rotor alignment requirement.

A. Operational

During normal operation, we require a steady rotation frequency (f_{HWP}) of 2 Hz or greater in order for the polarization

TABLE I. CHWP's numerical requirements and achieved values.

Parameter	Requirement	Achieved
Assembly outer diameter	≤950 mm	931 mm
Assembly height	≤246 mm	124.5 mm
Cryogenic stage mass	≤70 kg	66 kg
Clear aperture diameter	≥478 mm	490 mm
Rotor center alignment	≤5 mm	≤4.5 mm
Rotor temperature T_{rotor}	≤85 K	≤70 K
Stator temperature T_{stator}	≤70 K	≤60 K[a]
Thermal dissipation P_{stator}	≤3 W	≤1.6 W
Rotor thermalization time[b]	≤36 h	10 h
Rotation frequency f_{HWP}	2 Hz	0.5–3 Hz
Rotation stability Δf_{HWP}[c]	≤10 mHz	≤5 mHz
Encoded angle noise	≪3 μrad$\sqrt{s}$	0.07 μrad$\sqrt{s}$

[a]Achieved at a steady state when the rotor rotates at 2 Hz (Fig. 8).
[b]Lag time of rotor vs stator on initial cooldown (Fig. 7).
[c]The requirement is over the observation period of several years. The achieved stability is over 4 days (Fig. 12).

signal to be modulated faster than the $1/f$ knee of temperature fluctuations in the atmosphere.[41,64] In order to make efficient use of observing time, we require spin-up (spin-down) to (from) this rotation frequency to be achieved in less than 5 min. We also require the peak-to-peak stability of f_{HWP} to be better than 10 mHz during observations over a standard observation period of several years. Requirements are determined by operational conditions, such as the need to avoid noisy frequency regions in the TES power spectra or resonance frequencies of the mechanical structures in the cryostat.

B. Mechanical

For modularity, the CHWP rotation mechanism is designed to easily accommodate the front end, window-side, of the cryostat. This constrains the total envelope of the CHWP cryogenic components to be <950 mm in diameter and <246 mm in height along the optical axis. The total mass requirement of the CHWP, ≤70 kg, is not tightly constrained, as it is subdominant to the total suspended mass of the cryogenic stages supported by the primary cryo-mechanical truss.[65]

CHWP rotation can generate vibrations in the cryostat and heat up the focal plane's temperature, degrading detector gain stability and introducing $1/f$ noise. We require no measurable CHWP-induced resonant heating in the focal plane temperature. The vibrational performance is discussed in Sec. V D.

C. Optical

A clear aperture is one of the central requirements for the CHWP system. Special care is taken to prevent any optical interference from moving parts of the rotation mechanism, as any signal modulated at $4f_{HWP}$ mimics the incident polarization. To this end, we require all parts other than the sapphire stack to be circularly symmetric and to be outside of the −15 dB line of the 90 GHz beam (Fig. 2). The total power of the beam below the −15 dB level is estimated to be 0.52%. The −15 dB requirement is determined by a physical-optics simulation to ensure that sidelobe scattering from
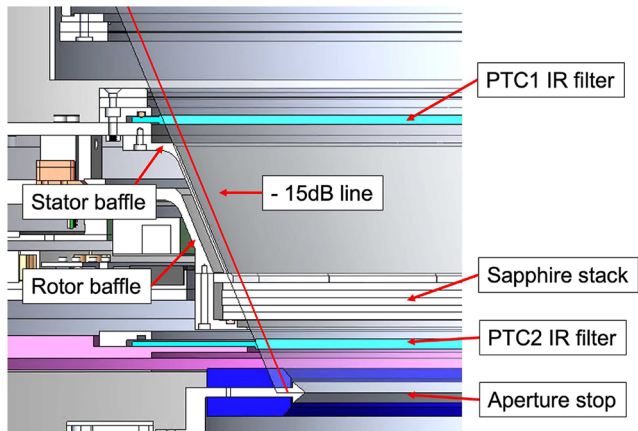
FIG. 2. A cross-sectional view of the CHWP system with the approximation of the −15 dB line of the 90 GHz beam, determined based on physical-optics simulations.[45]

the CHWP components is small compared to that from other optical elements of SAT.[45] The 90 GHz band is chosen to define the −15 dB line because it gives the most stringent optical requirements compared to other MF and UHF bands.

Given the SAT's 35° field of view and the diffraction limited beam, these requirements impose an approximated keep-out zone with an opening angle of about 23° extending skyward from the 420-mm diameter aperture stop (Fig. 2). The sapphire stack must be at least 490 mm in diameter at a distance of 40 mm away from the aperture stop, as close to the stop as possible while maintaining sufficient mechanical margin for the PTC2 alumina filter in between.

Finally, the misalignment of the rotor with the optical center must not exceed 5 mm during operation, as any larger misalignment would lead to physical interference or contamination of the beam.

D. Thermal

The rotor temperature is required to stay below 85 K to reduce thermal emission, requiring the thermal loading by the CHWP induced IR radiation incident on the PTC2 alumina filter to be subdominant to the total thermal loading on the PTC2 stage.[66] A lower temperature of the HWP optics reduces the fluctuation and non-uniformity of its emissivity and also helps to reduce the potential systematics in the observed polarization signal.

The stator temperature is required to be below 70 K, which is well below the critical temperature of the superconducting bearing, 95 K (Secs. IV B and V E). The power dissipation on the PTC1 stage is required to be subdominant to the total thermal loading on the PTC1 stage, and in addition, care is taken to effectively heat sink the CHWP stator to the PTC1 stage to reduce temperature gradients generated by the loading from the CHWP system during operation and to improve drive system efficiency by reducing the resistance of the motor drive coils. As such, we keep the thermal load on the PTC1 stage below ~3 W during operation. The low-power dissipation is an advantage not only for the cryogenic components but also for the room-temperature components, especially for the experiments conducted at the altitude of 5200 m, where convective air cooling is poor.

E. Data acquisition

Precise measurement of the rotation angle of the HWP is crucial for demodulation in the analysis pipeline. We require that the propagated noise equivalent temperature (NET) of the angular encoder be an order of magnitude smaller than the MF SAT NET goal: $1.4~\mu K\sqrt{s}$,[15] where we combine the sensitivity at 93 and 145 GHz to be conservative. Assuming a ~100 mK constant polarization induced by the vacuum window and the PTC1 alumina filter,[67] and following a similar calculation to that described in a study by Hill $et~al.$,[44] this imposes a limit of $3~\mu rad\sqrt{s}$ for the encoder white noise level. In addition to the low encoding noise, robustness
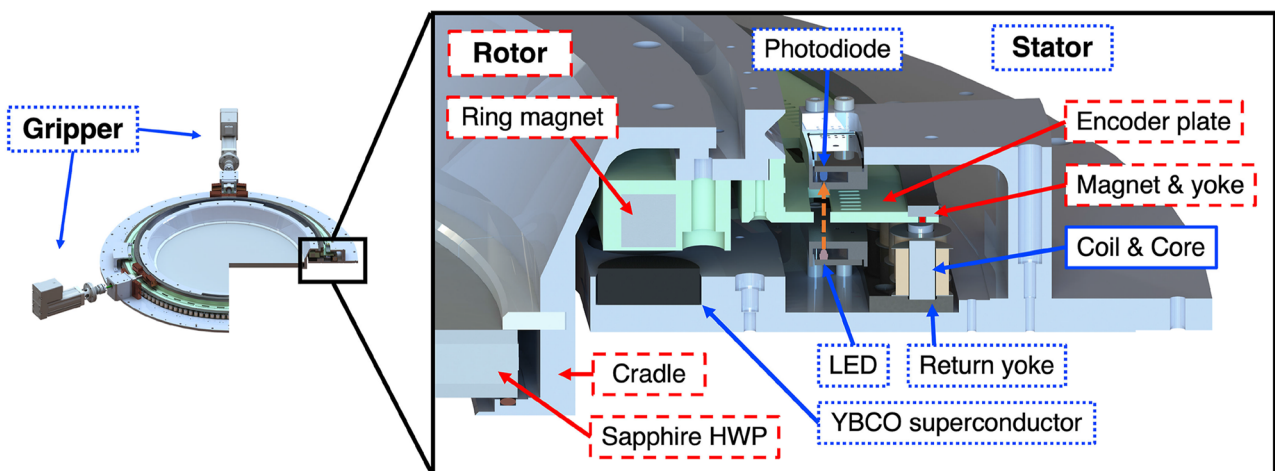
FIG. 3. Left panel: CAD views of the CHWP system. Right panel: magnified cross-sectional view of the rotation mechanism. The rotating components are labeled with red dashed boxes, and the stationary components are labeled with blue dotted boxes.

in encoding, such as a low rate of data packet loss and of glitches, is crucial.[68]

Due to the remote nature of the SO site, we also require that the CHWP system be capable of autonomous operation, including the capability of its diagnostic monitoring system to detect a power interruption to the cryostat and trigger an automatic shutdown procedure, braking and re-gripping of the rotor.

IV. DESIGN

This section describes the mechanical design of the rotation mechanism and highlights its novel aspects. The overall mechanism can be divided into five major components: the HWP, the superconducting magnetic bearing (SMB), the grippers, the motor, and the angle encoder.

As shown in Figs. 1 and 3, the non-rotating cryogenic components of the CHWP mechanism are built onto the most skyward flange of the PTC1 stage. The main non-rotating components are the superconductor ring, the motor system, and the encoder readheads. In addition, an aluminum shell on the outer diameter of the CHWP assembly provides a mounting flange for skyward optical components (the PTC1 stage IR blocking filters and related heat strapping) and creates a cold, well-regulated radiative cavity to help control the rotor temperature.

A. Sapphire stack mounting

The CHWP system employs an AHWP with a three-layer-sapphire stack sandwiched by AR layers. Hereafter, we refer to this optical element as the sapphire stack. It has a ~505 mm diameter, and the total thickness of all five layers is ~20 mm for the MF band. As shown in Fig. 4, the sapphire stack is held in an aluminum cradle. In the vertical direction, the sapphire stack is held along its circumference between a Spira[69] gasket (LS-08) and a series of nylon pads. Nylon is chosen for its low wear and friction at cryogenic temperatures.[70] In the radial direction, the sapphire stack is pressed by a 20° arc-shaped Spira gasket (SS-16). On the opposite side, it is held by two nylon stops, each placed at 120° from the gasket. The radial position is designed to be centered after cooldown, taking into account the contractions and the gasket spring constant.

The cradle is mounted on the rotor baffle, which is shielded from the beam by the stator baffle (Fig. 2). As discussed in Sec. III C, all components except for the sapphire stack, e.g., the cradle aperture and rotor baffle, are designed to intercept the diffracted 90 GHz beam at the −15 dB level or below when the rotor is at any position within the mechanical clearance. The stator baffle intercepts the diffracted beam at the −18.5 dB level at 90 GHz.

B. Superconducting magnetic bearing

The CHWP employs a 550 mm diameter superconducting magnetic bearing.[71] While SMBs have been demonstrated in other CHWP systems for CMB observations,[39,40,43,44,72] the SO SMB is the largest of its kind developed to date. The SMB is composed of a permanent ring magnet on the rotor and a ring of 61 or 53 disks of yttrium barium copper oxide[73] (YBCO) epoxied into an aluminum holder on the stator. The number of YBCO disks is different in two versions of SMBs to make the total levitation force similar, because the levitation force per one YBCO disk is different in two versions.
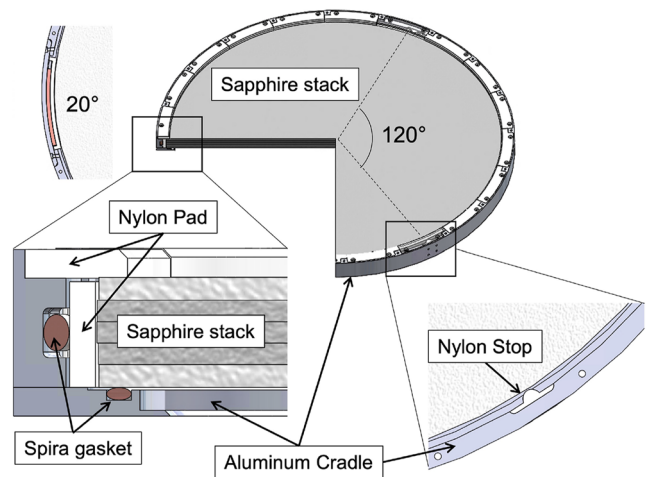

FIG. 4. CAD image of the sapphire stack held in an aluminum cradle. The sapphire stack is held in place vertically by Spira gaskets and nylon pads and radially by Spira gaskets and nylon stops.

YBCO is a type II superconductor with a transition temperature of ~90 K, below which the magnetic flux of the rotor is pinned in flux vortices in the disks, resulting in the loss of all but the rotational degree of freedom. The ring magnet of 550 mm inner diameter was manufactured by Shin-Etsu Chemical[74] and consists of 32 segments of neodymium (NdFeB; N52) fixed in a G10 enclosure. Care was taken in assembly to minimize gaps between the segments in order to maintain an azimuthally symmetric field. The number of YBCO disks and the number of magnet segments that make up the SMB are important design parameters, and making them relatively prime is critical to minimize vibration. This optimization of the SMB design and its vibration performance are discussed in Sec. V D. The friction and stability of this bearing were previously characterized in a study by Sakurai et al.[71]

C. Grippers

While the YBCO disks are above their transition temperature (~90 K), the rotor is not suspended by the flux-pinning effect and it is necessary to firmly grip it. This is accomplished by a grip-and-release mechanism, referred to hereafter as grippers. The grippers are a set of three linear actuators[75] with vacuum adapters manufactured by Huntington.[76] The actuator shafts mate to wedge tips mounted on the stator, which engage with a matching groove on the rotor when extended. This system allows for the precise and repeatable positioning of the rotor with respect to the rigid body of the SAT. The gripper design closely follows the design described in a study by Hill et al.,[44] with minor modifications. A single gripper can provide a pushing force that is more than twice the weight of the rotor; this is necessary to enable re-gripping and centering at any telescope elevation, as required in Sec. III C.

The three gripper arms each carry spring-loaded contacts or "touch probes" that align with copper flex-circuit traces on the rotor's outer diameter. These traces connect to a silicon diode thermometer on the rotor. When the grippers hold the rotor, two spring-loaded contacts touch the flex-circuit traces, measuring the
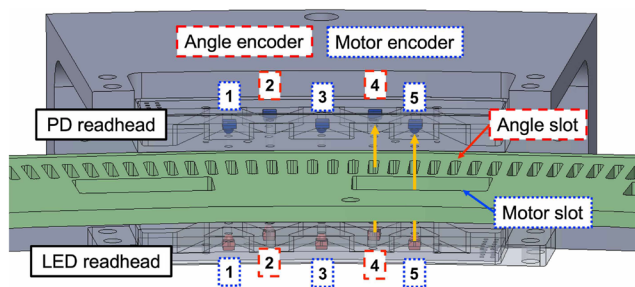
FIG. 5. Bird's eye view of one of the optical encoders and the encoder plate from inside top. The light emitted by the lower LEDs is chopped by the G10 encoder plate and detected by the PDs hanging over the encoder plate. The two angle encoders chopped by narrower slots are labeled in red, and the three motor encoders chopped by wider slots are labeled in blue.

rotor temperature. The measurement is only possible while the rotor is being held by the grippers. The measurement method can also be used to determine if the rotor is being held firmly.

D. Motor cryogenic assembly

The motor system that provides torque to the rotor is similar to that described in a study by Hill *et al.*,[44] with an increased number of coils due to the larger diameter of the SAT. The magnetic field from the 120 motor coils couples to the 80 magnet sprockets[77] on the edge of the encoder plate (Fig. 3), driving rotation. We employ two optical encoder assemblies, each with a set of five photodiodes[78] mounted on an arm that hangs over a G10 encoder plate on the rotor (Figs. 3 and 5). The LEDs are aligned with a matching set of five IR light-emitting diodes[79] (LEDs) located below the plate. The encoder plate is slotted at two different radii in order to chop the light emitted by the LEDs. The photocurrent signal chopped by the 40 wider slots drives the motor coils[80] by providing feedback through the motor drive electronics (Sec. IV E), while the signal chopped by the $570 - 1 = 569$ finer slots is fed to the encoder electronics for calculation of the rotation angle of the CHWP (Sec. IV F). One missing finer slot is a reference for marking the rotor's absolute rotation angle. Two encoder heads are installed at 180° from one another for redundant angle encoding. Data from both encoder heads can be combined to estimate the rotor's off-center displacement, as described in Appendix B.

E. Motor driver

The design of the motor drive electronics closely follows that used in a study by Hill *et al.*[44] Here, we highlight the two design improvements. First, a Proportional–Integral–Differential (PID) feedback system is used to further regulate the rotation frequency. For this system, a frequency-to-voltage circuit serves as an input to a PID controller,[81] which adjusts the drive voltage and modulates the motor torque. With the PID enabled, the frequency control system becomes closed loop and is able to account for unexpected changes to motor efficiency. PID parameters are chosen to minimize long-timescale variations.

Second, a phase compensation circuit is used to further improve rotation stability. While the CHWP rotates, the inductance of the motor coils and the counter-electromotive force distort the motor drive current against drive voltage. This distortion acts approximately as an effective phase delay to the motor drive current, and the phase delay increases with the rotation frequency, resulting in poor motor efficiency. The phase compensation circuit corrects for this phase delay. Simply compensating for the delayed phase significantly improves the motor efficiency. We implement a discrete phase compensation in 60° increments through the sign reversal and the phase swapping of the three-phase motor using relay modules. The use of the relay modules eliminates single-point failures and minimizes noise added to the motor coil drive feedback. Phase compensation with 60° increments is not always optimal but is easily achieved and provides sufficient control and efficiency. We automatically activate the phase compensation circuit when the rotation speed exceeds 1 Hz. The performance of the rotation drive control electronics and the evaluation of rotation efficiency are summarized in Secs. V B and V C, respectively.

F. Data acquisition

Data generated by the CHWP's cryogenic system are routed from the cryostat via four cables to a warm electronics box for processing. Acquisition of the rotor angular time stream requires cleaning and digitizing the raw encoder signals sent from the CHWP. This processing follows the method described in a study by Hill *et al.*[44]

The CHWP system also continuously records information from the motor driver, a Hall probe, and four silicon diode cryogenic thermometers. The diodes are placed on the YBCO superconductor ring, the sapphire stack mount on the rotor, the PTC1 filter plate, the PTC2 filter plate, and the rotor. These diodes are continuously monitored using a Lake Shore model 240.[82] A Hall probe[83] attached to the YBCO assembly continuously measures the magnetic field intensity around the superconductor (Fig. 21). The neodymium magnet in the rotor assembly is the primary magnetic source, and its field varies with changes in rotor temperature and displacement, enabling the Hall probe to monitor both of these properties.[84] The monitoring and control of the CHWP system are managed by the Observatory Control System.[85]

V. PERFORMANCE

We discuss the thermal and mechanical performances of three CHWPs evaluated at the University of Tokyo and in SAT cryostats at the University of California San Diego, Princeton University, and the Lawrence Berkeley National Laboratory (Fig. 6). Performance is evaluated using a dummy mass that brings the rotor mass to that expected with the full sapphire stack. The dummy mass is coated with epoxy to mimic the thermal conditions in the relevant IR frequencies.

A. Thermal

Figure 7 shows the rotor and stator temperatures during a cooldown process. Initially, the rotor is held by the grippers and is primarily cooled by conduction through the grippers' copper fingers. The rotor temperature lags behind the stator by 10 h, well within the 36 h requirement.

Once the YBCO disks become superconducting and the rotor temperature stabilizes, the rotor is ungripped and begins to levitate. Figure 8 shows the rotor temperature as a function of time, while it is floating (blue points) and when it spins at 2 Hz (red points)
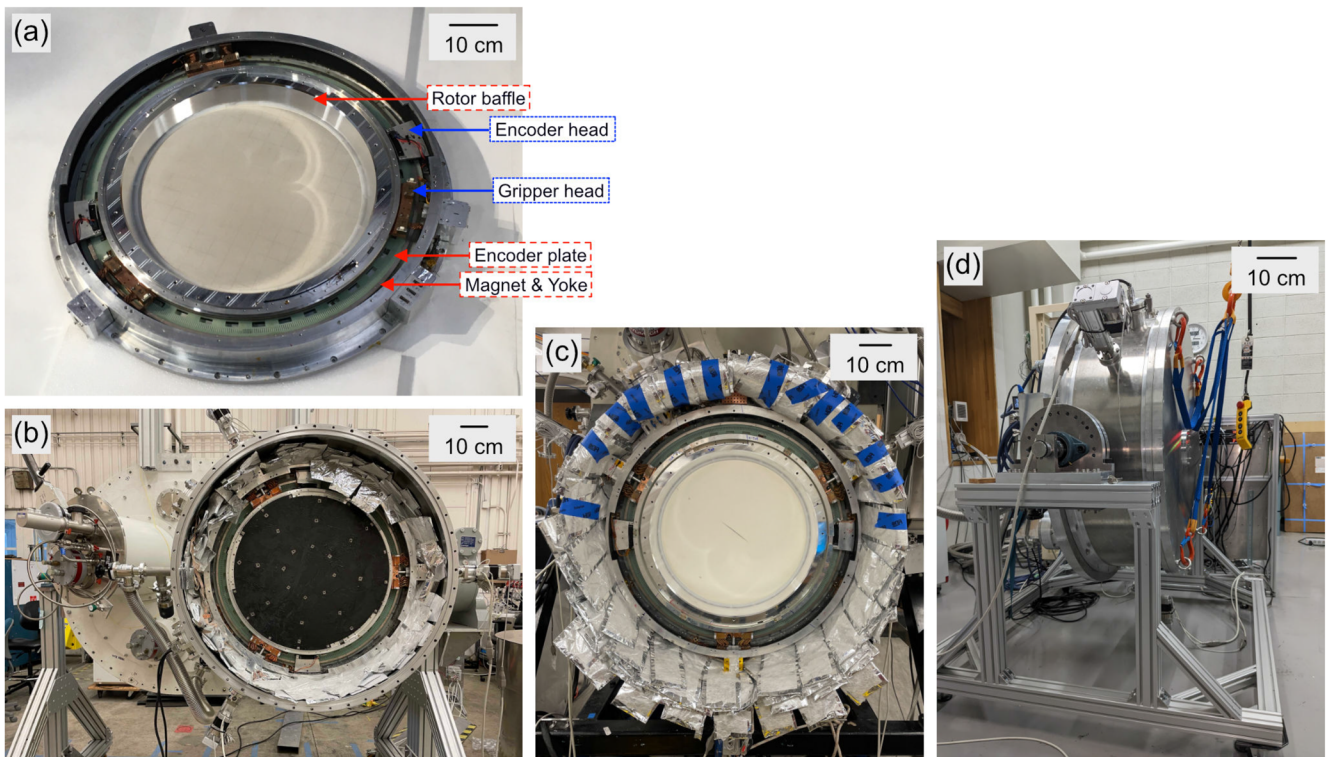
FIG. 6. CHWP rotation mechanisms during testing. Panel (a) shows the rotation mechanism with the sapphire stack for the SAT cryostat at UCSD. Panels (b) and (c) show the rotation mechanisms installed in the SAT cryostat at LBNL and Princeton University, respectively. In panel (b), the black object mounted on the rotor is a dummy mass, used to mimic the realistic mechanical and thermal conditions. Panel (d) shows the CWHP test cryostat at the University of Tokyo.

after temperature stabilization. In order to collect temperature data with the rotor spinning, its rotation is intermittently stopped and its temperature is measured using the gripper touch probes (Sec. IV C). This process is performed once every few hours with the duration of each touch not exceeding 60 s, leading to little disturbance in the rotor's temperature trend. The blue points inform us of optical loading where the IR loading is dominant, while the red points provide the estimates of the excess loading generated by rotation. Each set of points are fit by

$$T(t) = T_e + \Delta T \exp(-t/\tau), \qquad (3)$$

where T_e represents the estimated rotor temperature at a steady state, τ is the time constant, and ΔT is the difference between the initial and steady state temperatures. The steady state temperature of the CHWP rotating at 2 Hz is 70 K, which satisfies the requirement of $\leq$85 K. The time constants of the blue and red curves are 31 and 46 h, respectively.

Figure 9 shows the model for an ANSYS thermal simulation, which is used to further characterize the CHWP thermal cavity as well as the heat input to the rotor. For the simulation, we simply model the floating rotor surrounded by the PTC1 aluminum shell and the PTC1 and PTC2 alumina IR filters. Based on our measurements, we set the temperatures of aluminum shell and alumina filters in the simulation to 55, 60, and 4 K, respectively. The infrared

emissivity of the alumina IR filter is set to 0.8,[86] while that of the aluminum shell is set to 0.96. Here, the inside of the aluminum shell is covered with an infrared black body.[87] Since there is no physical contact, the rotor exchanges heat with other components only by thermal radiation. Figure 8 shows the simulated time series of the rotor temperature with a constant heat input to the floating rotor. By comparing the data with the simulation result, the heat input to the rotor is estimated to be 220 mW when the rotor is floating and 390 mW when the rotor is rotating at 2 Hz. The additional thermal loading on the PTC2 IR filter due to the presence of the rotor is estimated to be 120 mW, which is sufficiently small compared to the cooling capacity of the PTC2 stage, 1.8 W.

B. Rotation control

Figures 10 and 11 show the performance of the PID control and the phase compensation described in Sec. IV E. When the rotation PID feedback is on, the rotor accelerates to steady rotation at 2 Hz within 7 min and decelerates down to 0 Hz within 3 min. When phase compensation is used in conjunction with the PID, the spin-up time to steady rotation at 2 Hz is reduced to less than 4 min.

Figure 12 demonstrates the stability of the CHWP's rotation at 2 Hz over 4 days using PID control. The achieved stability of
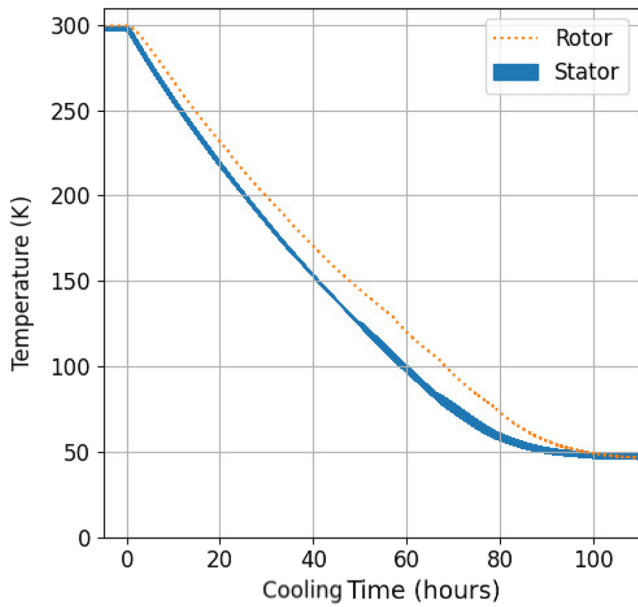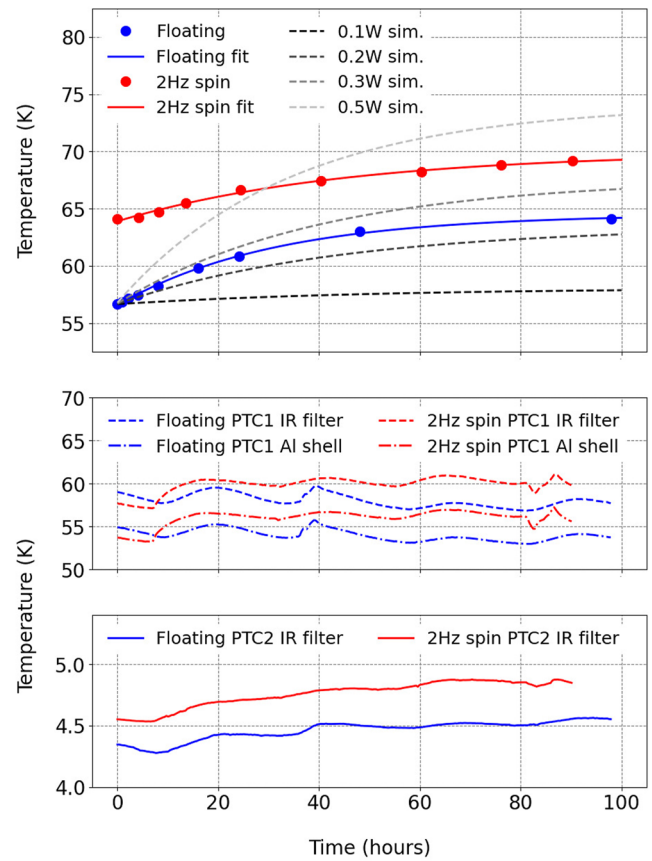
FIG. 7. Rotor and stator temperatures during cooldown. The rotor thermalizes within 10 h of the stator.

FIG. 8. Top panel: The rotor temperature profile while it is floating (blue points) and spinning at 2 Hz (red points), which are fit by Eq. (3) (solid lines). The black dashed lines show the ANSYS thermal simulation results with heat inputs of 0.1, 0.2, 0.3, and 0.5 W, respectively. The initial temperature of the simulation was set to the initial temperature of rotor when released from the grippers. The heat dissipation to the rotor is estimated by comparing the thermal equilibrium temperature between the fit result and the simulation. Middle panel: Colored dashed lines represent the temperatures of the alumina IR filter and aluminum shell. Bottom panel: PTC2 IR filter temperature profile while the rotor is floating (blue) and spinning at 2 Hz (red).

± 5 mHz is well within the required ± 10 mHz. Although not tested in-lab, the stability of the PID control loop over even longer timescales is expected to remain below the requirement. We additionally performed an in-lab azimuth scan to demonstrate stable operation of the CHWP under observation-like conditions. The receiver was held at a constant elevation angle of $50°$ and subject to an angular throw of $12°$, a constant scan velocity of $1°/s$, and a turnaround acceleration of $1°/s^2$. While the nominal SAT angular throw will be wider, more frequent turnarounds during this test enabled an evaluation of scanning effects on PID performance under more strenuous operating conditions.

Figure 13 shows a time stream of the measured rotation frequency during scanning where we observe a scan-synchronous modulation of the measured frequency (± 2 mHz). This is due to the fact that the encoders and SAT detectors are fixed in the telescope reference frame, the magnetically levitated CHWP is not. Thus, the measured modulation arises from the conservation of angular momentum of the CHWP about its rotation axis. The angular velocity of the CHWP during scanning is given by the following, of which the detailed derivation is described in Appendix A:

$$\dot{\chi}(t) = \bar{\dot{\chi}} - \dot{\phi}(t)\,\sin(\theta_{\text{el}}), \qquad (4)$$

where ϕ is the azimuth angle of the telescope, θ_{el} is the elevation angle of the telescope, and $\bar{\dot{\chi}}$ is the average angular velocity of the CHWP. The PID is tuned for longer-timescale stability and reacts little to the azimuthal scan modulation. This demonstrates that the accuracy of the encoding system and the stability of rotation frequency are well within the requirement, including the effect of scan modulation.

C. Rotation efficiency

Table II summarizes the thermal dissipation of the rotation mechanism to the stator and PTC1 stage. There are four primary sources of thermal dissipation from the CHWP: (a) Joule heating of the driving coils, where the phase compensation of the motor driver (Sec. IV E) plays an important role, (b) hysteresis loss in the SMB, (c) eddy current loss in the SMB, and (d) dissipation from the optical encoders. (a) is characterized by the impedance and the bias voltage of the motor coils, while (b) and (c) are characterized by fitting the spin-down curve, using the method described in a study by Sakurai et al.[71] As noted in Table II, (b) and (c) are dependent on the elevation angle, or the gravity vector direction. Lower elevation angles lead to a larger distance between the YBCO and the magnet ring of the rotor along the optical axis, resulting in a weaker and smoother magnetic field coupled to the YBCO, thus diminishing the loss from hysteresis and eddy currents. The total dissipation from the motor
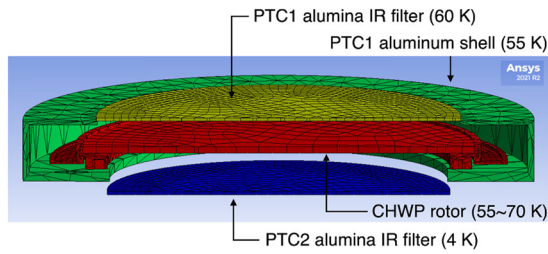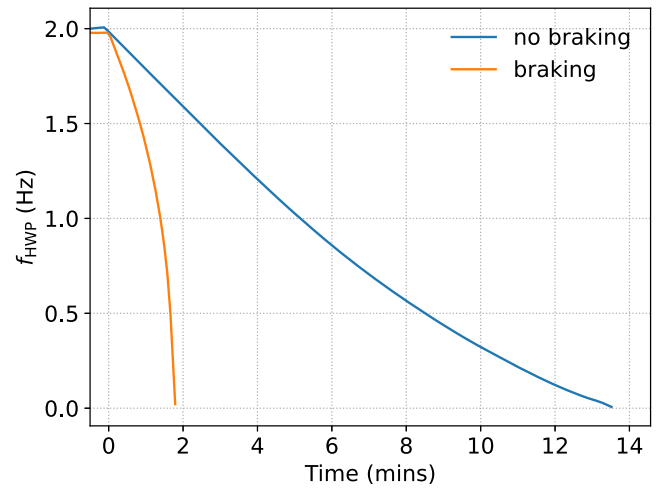
FIG. 9. ANSYS thermal model used to simulate the amount of thermal loading from the CHWP rotor to the PTC2 stage. The temperatures of the PTC1 aluminum shell and the PTC1 and PTC2 alumina IR filters are set at 55, 60 and 4 K, respectively. The rotor temperature is varied from 55 to 70 K to estimate the thermal loading on the PTC2 alumina IR filter. Image used courtesy of ANSYS, Inc.
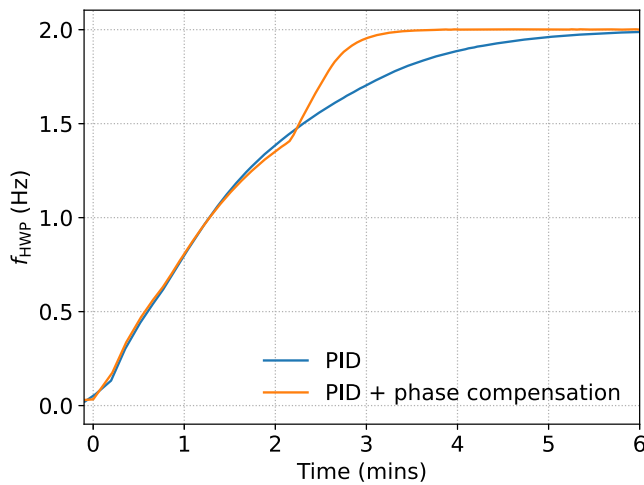

FIG. 10. Spin-up curves. The blue curve shows the spin-up curve with PID control. The rotation frequency stabilizes in ~7 min. The orange curve shows the spin-up curve with phase compensation activated at 2.2 min. With phase compensation, the rotation frequency stabilizes in ~4 min.

FIG. 11. Spin-down curves. The blue curve shows the spin-down curve of HWP without braking. Braking can bring the HWP to a stop in less than 2 min (orange curve).
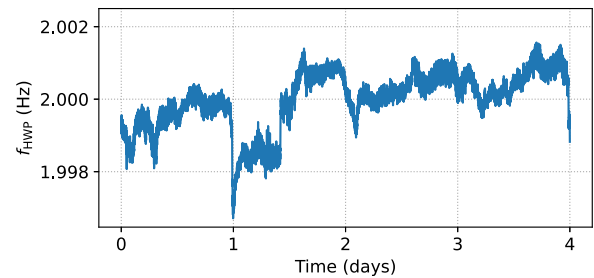
FIG. 12. Demonstration of the rotational stability of the CHWP at 2 Hz over 4 days using PID control.
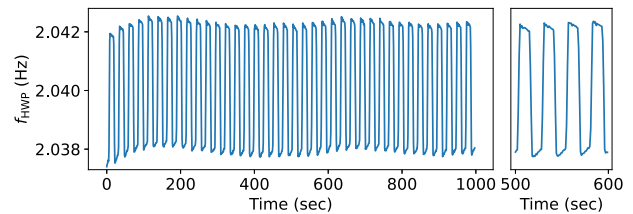
FIG. 13. Time stream of the measured HWP rotation frequency during the constant elevation scan of the SAT receiver at an elevation of 50°. The long timescale PID rotation control is enabled.

and SMB (a + b + c) is measured by comparing the loading on the PTC1 stage when the CHWP is operating and when it is not. The power dissipation of the optical encoders is mainly from the LEDs, which is estimated to be smaller than 1 W based on the bias current and voltage.

(a) is reduced by optimizing the phase compensation angle of the drive motor (Sec. IV E). The phase compensation angle was optimized using the power consumption of the motor driving voltage source,[88] which includes dissipation both inside and outside of the receiver. Figure 14 shows the power consumed by the voltage source as a function of the phase compensation angle of the drive motor. The power consumption with a 2-Hz rotation achieves minimum at 60°. With a motor drive phase compensation of 60°, the power consumption is reduced from 3.6 ± 1.0 to 0.8 ± 0.1 W, and the dissipation of the motor on the stator is reduced from 3.1 ± 1.0 to 0.5 ± 0.1 W. This results in a total power dissipation of ≤1.6 W, summing motor dissipation with that of the LEDs, which is below the requirement of 3 W.

As we discuss in Sec. V E, the elevation-dependent off-center displacement of the rotor induces a phase shift between the measurements of the two encoders. Because the motor drive voltage source uses feedback from the encoder to regulate its output (Sec. IV E), the rotation efficiency is dependent on this elevation-dependent phase shift and also on the rotation direction, resulting in the systematic variation in the Joule heat of the driving coils and the power consumption by the voltage source. As shown in Fig. 14, the rotation efficiency is sensitive to the phase shift of the motor when

phase compensation is not activated but is insensitive when 60° of phase compensation is activated. Therefore, the phase compensation enables us to achieve robust rotational efficiency regardless of changes to the off-center displacement and rotation direction. The systematic variation in the thermal dissipation of the rotation mechanism is negligible compared to the elevation-dependence of the PTC's cooling capacity.[89]

D. Vibration

The characteristic vibration frequencies of the SMB are key parameters for the vibrational performance of the CHWP. From the mass of the rotor and the displacement we evaluate in Sec. V E, the spring constants of the SMB parallel and perpendicular to the optical axis are estimated to be 5.2(8.4)×10^5 and 9.1(17) ×10^4 N/m, respectively, for 48(61) YBCO tiles. From these values, we determine the corresponding characteristic vibrational frequencies to be 7(9) and 9(13) Hz, respectively, which are in agreement with the results of Sakurai *et al.*[71]

The primary instrumental parameter that impacts the vibrational performance is the number of YBCO disks of the SMB. Throughout our evaluation of the SAT's susceptibility to CHWP induced vibrations, our design of the SMB evolved from 48 disks to 53 or 61. This section presents their comparison. We employ two methods to characterize vibration, one by using a three-axis accelerometer[90] mounted on the cryostat near the rotation mechanism and the other by measuring the temperature increase of the 100-mK focal plane stage while sweeping through CHWP rotation frequencies.

Figure 15 shows the spectrogram of the vibration parallel to the optical axis. We do not observe significant vibration perpendicular to the optical axis. Vibrations were measured at frequencies equal to f_{HWP} multiplied by the number of coils (=120) or the number of YBCO disks (=48, 53) multiplied by an integer. In the 48-disk setup, the 96th harmonic of f_{HWP} was the largest vibrational mode. 96 is the least common multiple of the number of YBCO disks (=48) and the number of NdFeB magnet segments (=32), and this relationship yielded vibrational coupling that produced higher amplitude vibration. In the 53-disk setup, the number of YBCO disks and the number of NdFeB magnets are relatively prime (do not have common divisors larger than 1) and we did not observe vibrational mode associated with their coupling.

The influence of vibration on the focal plane temperature in two representative SMBs with different numbers of YBCO disks is

shown in Fig. 16. The rotation of CHWP was monotonically swept in frequency from 0.5 to 2.3 Hz over a 12 h duration while measuring the temperature of the cryogenic stages. Since these two SMBs are tested in SATs with different instrumentation, a direct comparison of the thermal sensor noise is not possible; however, the resonant heating response observed in a 48-disk setup is not seen in a 53-disk setup.

E. Rotor alignment and displacement

There are two degrees of freedom that we consider important for the alignment of the CHWP rotation mechanism: alignment along the optical axis, involving displacement perpendicular to the plane of the SMB, and center alignment, involving displacement along the SMB plane. In this section, we discuss the alignment performance along these degrees of freedom, in addition to the effect of temperature on alignment. The quality of the rotor alignment is determined both by the initial centering established by the grippers and by the stiffness of the SMB.

Because the magnetic flux-pinning acts as a restoring force with a finite spring constant, when the rotor is released from the grippers, it displaces due to gravity, finding a new equilibrium position that depends on the elevation angle. Due to its azimuthal symmetry, the SMB is most stiff along the optical axis.[40] The off-center displacement produces a phase shift between the two angle encoders, resulting in a difference between the calculated and actual rotational angle and the encoded angle. Therefore, the evaluation of off-center displacement is particularly important.
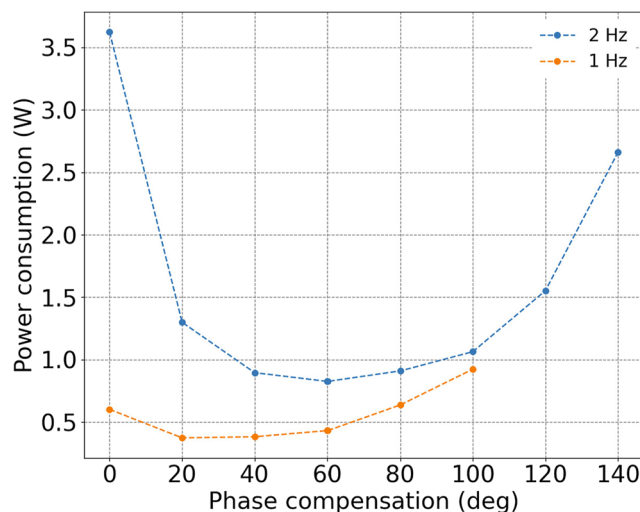

FIG. 14. Power consumption of the voltage source of the three-phase motor as a function of phase compensation angle. The blue (orange) line is for the rotor rotating at 2 (1) Hz. A digital phase compensation circuit implemented by a microcontroller is used to apply an arbitrary amount of phase compensation and to explore the motor efficiency as a function of the compensated phase. We find that the near-optimal compensation angle is 60°, which can be achieved by discrete phase compensation. As such, we adopt the simpler and more robust discrete phase compensation in the actual implementation. The digital phase compensation circuit is used only for this investigation.

TABLE II. Dissipation of rotation mechanism on stator, PTC1 stage.

Motor	Joule heat of driving coils	0.4 ± 0.1 (2.6 ± 1.0 W)[a]
SMB	Hysteresis loss of SMB	0.083/0.084 W[b]
	Eddy current loss of SMB	0.058/0.099 W[b]
	Total	0.5 ± 0.1 W (3.1 ± 1.0 W)[a]
Encoder	Power dissipated by LEDs	≤1 W[c]

[a]Dissipation when phase compensation is activated (not activated). The error bar is the systematic variation due to its dependence on the elevation angle and the rotation direction.
[b]Dissipation at an elevation of 50°/90°.
[c]10 LEDs are biased with 50 mA and 2 V.

The stiffness of the SMB is the product of the critical density current of the YBCO, the magnetization of the NdFeB permanent magnet ring, and a constant determined by the geometry of the SMB. A temperature increase from 50 to 85 K results in ~90% reduction in the critical density current[91] and ~10% reduction in the magnetization.[92] Thus, by measuring the temperature dependence of the rotor displacement, we can determine the temperature dependence of the stiffness and obtain the maximum operating temperature of the SMB.

Each of the three primary CHWP alignment considerations can be evaluated independently. Alignment along the optical axis is characterized at 50 K with the methods described in Appendix B. The largest displacement occurs at an elevation angle of 90°, resulting in a displacement of 2.0 ± 0.3 mm, which is well within the designed clearance of 5 mm.

The center alignment is evaluated using the method described in Appendix B. Figure 17 shows the measured off-center displacement at different elevation angles and for SMBs with different numbers of YBCO disks. The off-center displacement was measured seven times at an elevation of 90°, and the initial alignment accuracy was found to be ≤1 mm. Inaccurate initial centering by the grippers while cooling through the YBCO transition produces a non-zero displacement at an elevation of 90°. As Fig. 17 shows, the off-center displacement decreases as the number of YBCO disks is increased and is smaller than 3.5 mm with 61 YBCO disks at elevation angles larger than 20°.[93] This satisfies the requirement for optical and mechanical clearance of ≤5 mm even when combined with the initial alignment accuracy ≤1 mm.
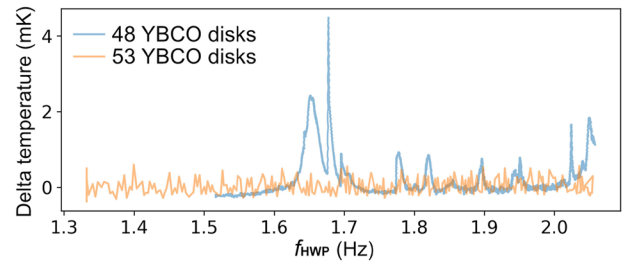
FIG. 16. Comparison of the effect of vibration on the focal plane temperature in two SMBs with different numbers of YBCO disks. The nominal focal plane temperature is 100 mK.

Finally, the temperature dependence of the displacement (Fig. 18) is evaluated to determine the maximum operating temperature through the following three steps:

1. The temperature of the YBCO is gradually increased to 85 K. The off-center displacement is constant up to 70 K but rapidly increases after reaching 70 K.
2. The YBCO temperature is gradually lowered from 85 K. The off-center displacement does not change throughout this process.
3. The YBCO temperature is gradually increased to observe where the off-center displacement starts to increase again. The off-center displacement remains the same up to ~85 K but
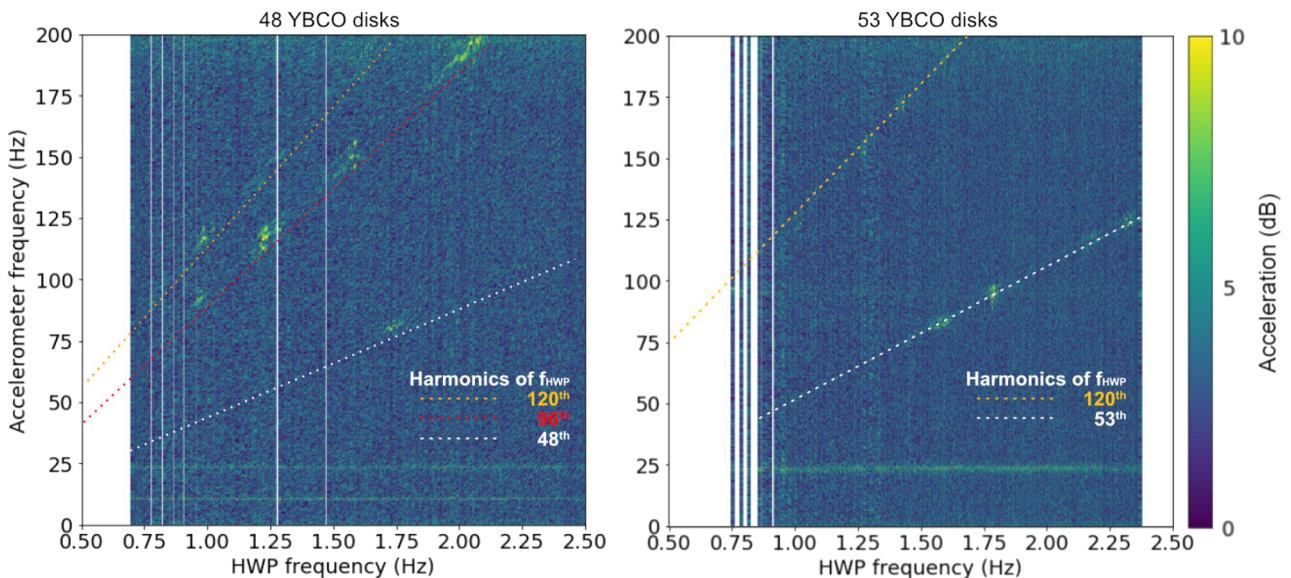
FIG. 15. Comparison of the vibration of the SMB with different numbers of YBCO disks. The color scale is normalized by the noise level of the accelerometer. Vibration is observed at f_{HWP} multiplied by an integer times a common multiple of the characteristic numbers of the SMB: the number of ring magnet segments (=32), the number of YBCO disks (=48, 53), or the number of coils (=120). The vibration observed on the 48-disk SMB at f_{HWP} multiplied by the least common multiple of the number of YBCO disks and ring magnet segments (=96) is not observed on the 53-disk SMB.
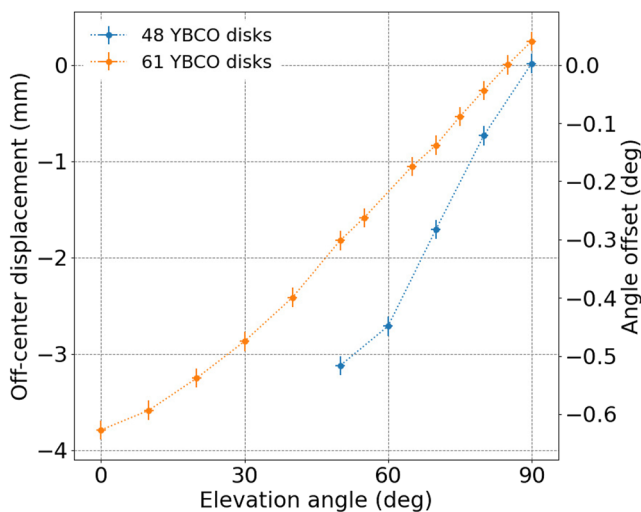
begins to rapidly increase when the temperature rises above 85 K.

With this test, we find that the maximum operating temperature of the SMB is not the transition temperature of the YBCO (~95 K) but 70 K. This temperature requirement is satisfied with sufficient margin under the normal operating conditions of our system. We additionally find that, if the off-center displacement occurs due to the temperature increase, it cannot be restored by simply lowering the temperature of the YBCO. Once the displacement has occurred, it is retained unless the SMB is brought to a higher temperature. In order to re-center the rotor, it is necessary to grip it at the center and warm up the YBCO disks above their transition temperature, followed by a re-cooling to flux-pin the rotor in the correct position.
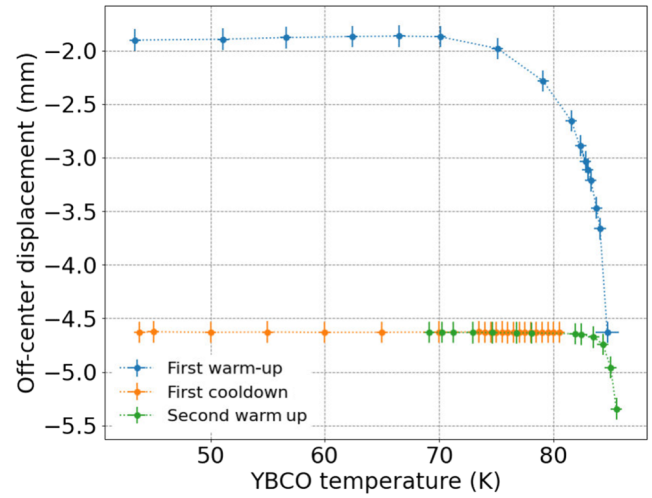
F. Angle encoding accuracy

There are two primary sources of angle encoding inaccuracy: the timing jitter of the data acquisition system and noise in the encoder readout. The total noise should correspond to less than $3\,\mu\mathrm{rad}\sqrt{s}$ (Sec. III E).

We first discuss timing jitter and, more specifically, the uncertainty of CHWP angle timestamp assignment. A BeagleBone Black microcontroller[94] acquires the encoder data and assigns their timestamps based on its internal 200 MHz free-running clock (Sec. IV F). Since the internal clock has long-timescale frequency drifts, the timestamps must be corrected by referencing the microcontroller to the SAT's master clock, which also synchronizes with detector timestreams. The microcontroller receives the master clock signal as IRIG-B[95] frame and position identifiers at a rate of 10 times per second. There are uncertainties, including jitter and data loss, in the measurement of the encoder and IRIG-B pulses; therefore, we determine the CHWP angle after data acquisition by analyzing the full

FIG. 18. Off-center displacement when the YBCO temperature is increased and decreased to evaluate the maximum operating temperature of the SMB. During measurements, the rotor is continuously rotating at 2 Hz and the elevation angle is 50°.

FIG. 17. Off-center displacement of the rotor at different elevation angles and different numbers of YBCO disks. The elevation angle of 90° refers to pointing at zenith (Fig. 20). The angle offset is an additional measured angle difference between the two encoders due to the off-center displacement of the rotor [Eq. (B1)].

history of the internal timestamps for the two signals. The corrected timestamp is expressed as

$$\hat{t} = t_{\mathrm{true}} + \Delta t_{\mathrm{clk}}, \tag{5}$$

where Δt_{clk} is the uncertainty in the correction after synchronizing the encoded angle timestamps to IRIG-B time. The effect of timing jitter on angle encoding accuracy is evaluated by the power spectral density (PSD) of Δt_{clk}, which is determined by the relative time difference between the internal clock and IRIG-B time,

$$\Delta t_{\mathrm{diff}} = t_{\mathrm{bbb}}|_{t=t_{\mathrm{true}}-\Delta t_{\mathrm{IRIG}}} - t_{\mathrm{true}} \simeq \Delta t_{\mathrm{bbb}} - \Delta t_{\mathrm{IRIG}}, \tag{6}$$

where t_{bbb} is the internal clock time, Δt_{bbb} is the drift of internal clock relative to IRIG-B, and Δt_{IRIG} is the timing jitter resulting from the detection of IRIG-B pulses. Since Δt_{bbb} and Δt_{IRIG} are independent, the PSD is

$$\mathrm{PSD}(\Delta t_{\mathrm{diff}}) = \mathrm{PSD}(\Delta t_{\mathrm{bbb}}) + \mathrm{PSD}(\Delta t_{\mathrm{IRIG}})$$
$$= A f^{-\alpha} + \sigma_{\mathrm{IRIG}}^2/10 \quad (\sec^2\ \sec), \tag{7}$$

where A and α are the $1/f$ noise parameters of Δt_{bbb} and σ_{IRIG}^2 is the noise variance in terms of 10 Hz IRIG-pulse detection. The blue dashed curve in Fig. 19 shows the corresponding angle jitter due to the timing jitter constructed from Eq. (7) multiplied by the angular velocity. The $1/f$ noise is given by Δt_{bbb}, and the white noise level is determined by Δt_{IRIG}. The corrected time, $\hat{t}$ [Eq. (5)], is constructed by synchronizing the internal clock to the IRIG-B
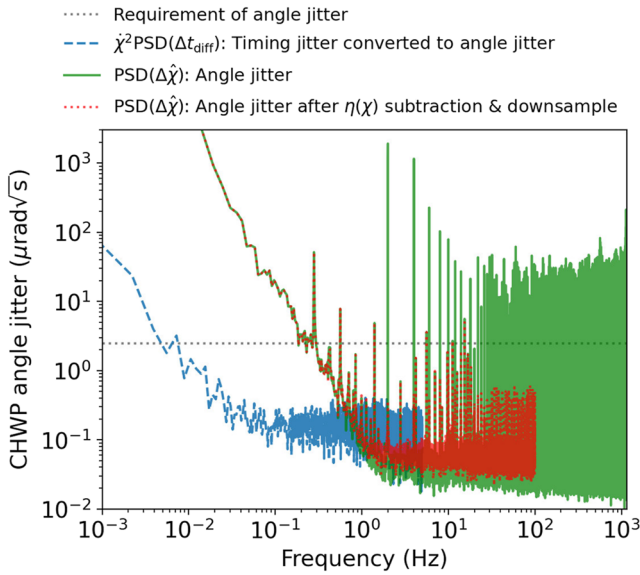
FIG. 19. A measurement of the angle encoder performance over 1 h. The CHWP is constantly rotating at 2 Hz. The high frequency peaks in the raw PSD ($\Delta\hat{\chi}$) are due to the non-uniformity of the encoder slot pattern, $\eta(\chi)$. The residual peaks after the $\eta(\chi)$ subtraction and down-sampling correspond to true fluctuation in the rotation angle, which are caused by vibrations of the PTC and the effects of the PID rotation control. The requirement applies only to the white noise level of the angle jitter.

signal at a frequency of f_{sync} by linear interpolation. Therefore, the PSD of the uncertainty in the corrected time Δt_{clk} is approximately expressed as

$$\text{PSD}(\Delta t_{\text{clk}}) \simeq \begin{cases} \sigma_{\text{IRIG}}^2/10, & f \leq f_{\text{sync}}/2, \\ Af^{-\alpha}, & f \geq f_{\text{sync}}/2. \end{cases} \quad (8)$$

At frequencies below the synchronization Nyquist frequency ($f_{\text{sync}}/2$), the timestamp correction eliminates the $1/f$ noise and the white noise of the IRIG detection jitter limits the timing accuracy. At frequencies above $f_{\text{sync}}/2$, the timing accuracy still relies on the microcontroller's internal clock, resulting in the small amount of time drift. As shown in Fig. 19, the angle jitter due to the timing jitter of the corrected time satisfies the requirement at all frequencies.

Next, we evaluate the encoder readout noise. We place an upper limit on encoder readout noise using the encoder data and the CHWP's smooth rotation. The encoded CHWP angle is

$$\hat{\chi}(t_{\text{true}}) = \chi_{\text{true}}(\hat{t} + \Delta t_{\text{enc}}) + \eta(\chi_{\text{true}}), \quad (9)$$

where $\hat{\chi}$ is the encoded rotation angle of the CWHP, χ_{true} is the true rotation angle of the CHWP, and Δt_{enc} is the timing jitter that arises from the detection of photo-encoder pulses. $\eta(\chi_{\text{true}})$ is the non-uniformity of the encoder slot pattern. The CHWP angle jitter is defined by subtracting the smooth rotation,

$$\Delta\hat{\chi} = \hat{\chi}(t_{\text{true}}) - \overline{d\hat{\chi}/dt_{\text{true}}} \cdot t_{\text{true}}$$
$$\simeq \Delta\chi_{\text{true}} + \dot{\chi}\Delta t_{\text{clk}} + \dot{\chi}\Delta t_{\text{enc}} + \eta(\chi_{\text{true}}), \quad (10)$$

where $\Delta\chi_{\text{true}}$ is the true drift of the CHWP angle that we would like to measure. Since $\Delta\chi_{\text{true}}$, Δt_{clk}, Δt_{enc}, and $\eta(\chi_{\text{true}})$ are independent, the PSD of the CHWP angle jitter is

$$\text{PSD}(\Delta\hat{\chi}) \simeq \text{PSD}(\Delta\chi_{\text{true}}) + \dot{\chi}^2\text{PSD}(\Delta t_{\text{clk}}) + \dot{\chi}^2\text{PSD}(\Delta t_{\text{enc}}) + \text{PSD}(\eta(\chi_{\text{true}})), \quad (11)$$

where

$$\dot{\chi}^2\text{PSD}(\Delta t_{\text{enc}}) \simeq \frac{\dot{\chi}^2\sigma_{\text{enc}}^2}{f_{\text{HWP}} \times 1140} \quad (\text{rad}^2 \ \text{sec}) \quad (12)$$

and σ_{enc}^2 is the noise variance in terms of the encoder-pulse detection timing. There are 1140 pulses per revolution. The green solid curve in Fig. 19 shows Eq. (11) when the CHWP rotates at 2 Hz. The $1/f$ component is the true drift of the CHWP angle, $\Delta\chi_{\text{true}}$. The white noise level is determined by Δt_{enc} and is well below the requirement. The peaks at the harmonics of f_{HWP} arise from $\eta(\chi_{\text{true}})$. f_{sync} is chosen to be 1 Hz to ensure that the timing jitter becomes subdominant to the drift of the CHWP angle at all frequencies.

To demodulate the TES detector timestream sampled at 200 Hz, the raw CHWP angles sampled at $1140 \times f_{\text{HWP}}$ Hz need to be down-sampled. In this procedure, the peaks at the higher harmonics of f_{HWP} must be subtracted so as not to contaminate the down-sampled angular timestream. The non-uniformity of the encoder slot pattern, $\eta(\chi_{\text{true}})$, is estimated by time averaging $\Delta\hat{\chi}$ for each angle step of the encoder signal as

$$\eta(\chi_{\text{true}}) \simeq \overline{\Delta\hat{\chi}} \quad \text{for each } (\hat{\chi} \mod 2\pi). \quad (13)$$

The red dotted curve in Fig. 19 shows the angle jitter after the slot pattern subtraction and down-sampling. The residual peaks at the harmonics of f_{HWP} are due to the slow modulation of the rotation-synchronous fluctuations of $\dot{\chi}$. The achieved noise level is $0.07 \ \mu\text{rad}\sqrt{s}$, which is more than one order of magnitude lower than the requirement.

VI. CONCLUSION

We have presented the requirements, design, and performance of the CHWP rotation mechanism for the Simons Observatory Small Aperture Telescopes. This work advances the field of cryogenic polarization modulators for mm-wave and sub-mm astronomical observations by introducing the largest diameter CHWP constructed to date. The aperture size of the CHWP system was previously constrained by the size of the rotor's magnet ring. By overcoming the manufacturing limitations of the SMB and optimizing the optical design, the size of the system is now limited by the largest available size of sapphire plate.[96] This work has also advanced the CHWP rotation drive techniques to improve operational efficiency and introduced new methodologies for characterizing CHWP systems, which enabled an improvement in the SMB to reduce vibration and evaluate the rotor displacement.

The CHWP for LFs is currently under development and will have different design parameters. The center alignment of the rotor will be more challenging since the LF HWP sapphire stack is a factor of 3–4 thicker and thus ~15 kg heavier than the MF HWP. Meanwhile, the LF band enjoys significantly less atmospheric fluctuations

than the higher frequency bands, and thus, the requirements on the CHWP rotation frequency can be relaxed.

Three CHWPs have been built and evaluated for three SATs, and three additional CHWPs are planned to be built. The CHWP performance satisfies all requirements, including a 478 mm clear aperture, a rotor temperature of <70 K, a stator temperature of <60 K, <1.6 W of dissipation during continuous operation, rotation frequencies up to 3 Hz, rotation stability within 5 mHz, rotor alignment within 5 mm, and 0.07 μrad$\sqrt{s}$ of the encoded angle noise. The presented CHWPs are expected to be deployed to the Chilean observation site and to see first light in 2023. This development contributes not only to the SO project but also to the design and trade study for future experiments, such as CMB-S4.[97,98]

AUTHOR DECLARATIONS

Conflict of Interest

The authors have no conflicts to disclose.

Author Contributions

K. Yamada: Methodology (equal); Resources (equal); Investigation (equal); Validation (equal); Software (equal); Writing – original draft (lead). **B. Bixler**: Methodology (equal); Resources (equal); Investigation (equal); Validation (equal); Software (lead); Writing – original draft (supporting). **Y. Sakurai**: Conceptualization (equal); Methodology (equal); Resources (equal); Investigation (equal); Validation (equal); Software (equal); Funding Acquisition (supporting); Writing – original draft (equal). **P. C. Ashton**: Conceptualization (equal); Methodology (equal); Resources (equal); Investigation (equal); Validation (equal); Writing – original draft (equal).

J. Sugiyama: Methodology (equal); Resources (equal); Investigation (equal); Validation (equal); Software (supporting); Writing – original draft (supporting). **K. Arnold**: Project Administration (equal); Supervision (equal); Funding Acquisition (supporting). **J. Begin**: Investigation (supporting); Validation (supporting); Writing – review & editing (supporting). **L. Corbett**: Investigation (supporting); Validation (supporting). **S. Day-Weiss**: Investigation (supporting); Validation (supporting); Writing – original draft (supporting). **N. Galitzki**: Supervision (supporting); Investigation (supporting); Validation (supporting); Writing – review & editing (supporting). **C. A. Hill**: Conceptualization (equal); Methodology (supporting); Software (equal); Writing – review & editing (supporting). **B. R. Johnson**: Supervision (supporting); Funding Acquisition (supporting); Writing – review & editing (supporting). **B. Jost**: Writing – review & editing (supporting). **A. Kusaka**: Project Administration (equal); Supervision (lead); Conceptualization (equal); Investigation (supporting); Validation (supporting); Funding Acquisition (lead); Writing – original draft (supporting). **B. J. Koopman**: Software (equal). **J. Lashner**: Software (equal). **A. T. Lee**: Project Administration (equal); Conceptualization (supporting); Supervision (supporting); Funding Acquisition (supporting). **A. Mangu**: Investigation (supporting); Validation (supporting). **H. Nishino**: Software (equal); Writing – review & editing (supporting). **L. A. Page**: Project Administration (equal); Conceptualization (supporting); Supervision (supporting); Investigation (supporting); Validation (supporting); Funding Acquisition (supporting); Writing – review & editing (supporting). **M. J. Randall**: Investigation (supporting); Validation (supporting). **D. Sasaki**: Investigation (supporting); Software (supporting); Writing – review & editing (supporting). **X. Song**: Investigation (supporting); Validation (supporting). **J. Spisak**: Investigation (supporting); Validation (supporting); Writing – original draft (supporting). **T. Tsan**: Investigation (supporting); Validation (supporting). **Y. Wang**: Investigation (supporting); Validation (supporting). **P. A. Williams**: Investigation (supporting); Validation (supporting).

DATA AVAILABILITY

The data that support the findings of this study are available from the corresponding authors upon reasonable request.

APPENDIX A: SCAN SYNCHRONOUS MODULATION OF HWP ROTATION

Here, we derive the scan modulation of the angular velocity of the CHWP [Eq. (4)]. Figure 20 shows the schematic diagram of the rotating CHWP on the scanning telescope. The coordinate system can be taken as shown, without the loss of generality. We define r and θ as the cylindrical coordinates of the rotor and $\rho(r, \theta)$ as the rotor mass density, which is symmetric about θ. The angular momentum of the rotating CHWP is

$$L_{\mathrm{HWP}} = \dot{\chi} \iint r \, dr d\theta \, \rho r^2 = \dot{\chi} I, \tag{A1}$$

where I is the moment of inertia of the rotor.

Next, we calculate the angular momentum induced by the scanning telescope. Let r_0 be the radial distance from the axis of the scan to the center of the rotor. We assume that the CHWP bearing is

27 February 2024 19:16:45

infinitely rigid. This means that the net angular momentum contribution from the telescope scan is only along the direction of the rotor's rotation axis. As shown in Fig. 20, the angular momentum at each point of the rotor induced by the telescope scan is

$$
\begin{aligned}
\delta L_{\text{scan}} &= \hat{n}_{\text{HWP}} \cdot \left(\vec{r} \times \rho \vec{v} \right) \\
&= \begin{pmatrix} \cos \theta_{\text{el}} \\ 0 \\ \sin \theta_{\text{el}} \end{pmatrix} \cdot \left\{ \begin{pmatrix} r \sin \theta_{\text{el}} \cos \theta \\ r \sin \theta \\ -r \cos \theta_{\text{el}} \end{pmatrix} \times \rho \dot{\phi} \begin{pmatrix} -r \sin \theta \\ r_0 + r \sin \theta_{\text{el}} \cos \theta \\ 0 \end{pmatrix} \right\} \\
&= \rho \dot{\phi} \left(r_0 r \cos \theta + r^2 \sin \theta_{\text{el}} \right),
\end{aligned} \tag{A2}
$$

where ϕ and θ_{el} are the azimuth and elevation angles of the telescope, respectively. The total angular momentum is obtained by integrating over the rotor as

$$
L_{\text{scan}} = \iint r \, dr d\theta \, \delta L_{\text{scan}} = \dot{\phi} \sin \theta_{\text{el}} I. \tag{A3}
$$

From the conservation law of angular momentum, the following equation holds:

$$
L_{\text{scan}} + L_{\text{HWP}} = \text{const.} \tag{A4}
$$

Thus, Eq. (4) holds.

APPENDIX B: MEASUREMENT OF THE DISPLACEMENT OF ROTOR

Here, we elaborate on the methods used to make the displacement measurements summarized in Sec. V E. Displacement measurements along the optical axis are made using the gripping mechanisms (Sec. IV C) and a Hall probe (Sec. IV F) installed below the rotor's magnet ring. The measurement begins by pointing the receiver at an elevation of 90° and fully gripping the rotor. The actuators controlling the gripper positions are then retracted, allowing the rotor to sink along the optical axis. The gripper head geometry is designed such that the retraction distance corresponds directly to the rotor displacement, and changes in the Hall probe's measured field are monitored. The total displacement of the rotor is estimated from the distance the grippers have moved while the Hall

probe changes linearly. Figure 21 shows a schematic of the measurement setup and the measured magnetic field of the rotor magnet as the grippers are gradually retracted. The systematic error of the displacement is ±0.3 mm, resulting from changes in the Hall probe sensitivity and the rotor magnet's field caused by temperature drifts during the measurement.

The off-center displacement is calculated by the measured additional angle offset between a pair of encoders placed 180° from one another as shown in Fig. 22. The additional angle offset is

$$
d\chi_j = \pi f_{\text{HWP}j} \left(t_j^0 - t_{j+570}^1 \right), \tag{B1}
$$

where t_j^i is the timing when the i-th encoder reads the j-th encoder slot and

$$
f_{\text{HWP}j} = \frac{1}{1140 \left(t_j^0 - t_{j+1}^0 \right)} = \frac{1}{1140 \left(t_j^1 - t_{j+1}^1 \right)} \tag{B2}
$$

is the rotation frequency. Since the total number of encoder slots is 1140, the slot 570 positions away is at the opposite side of the encoder plate. If the CHWP is completely centered, $d\chi_j$ is always zero. If there is an off-center displacement of the rotor perpendicular to the line connecting the encoders, diametrically opposite slots will travel different distances between detection, resulting in a time delay that can be converted to the angle offset, $d\chi_j$. The pair of encoders are synchronized by the shared IRIG-B reference signal described in
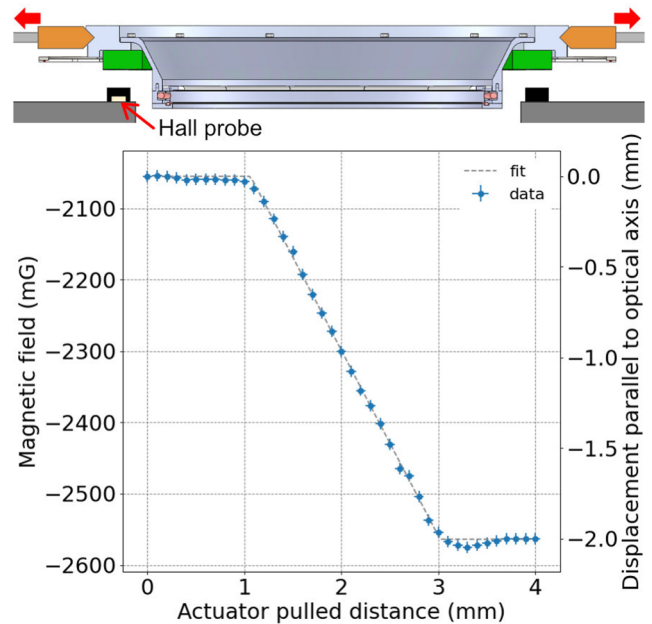
FIG. 21. Top panel: Schematic diagram of the measurement setup for the rotor displacement along the optical axis. The Hall probe is located right below the magnet ring to measure the relative displacement of the rotor. The grippers are completely clear of the rotor when retracted 9 mm. Bottom panel: Measurement of the displacement along the optical axis. From 0 to 1 mm, the rotor is not moving due to the play in the joints of the grippers. From 1 to 3 mm, the rotor is sliding down the wedge of the gripper heads. From 3 mm onward, the rotor is floating.
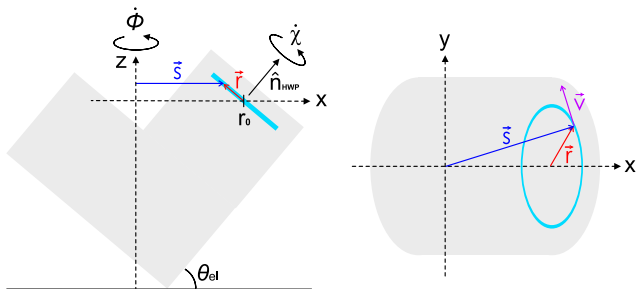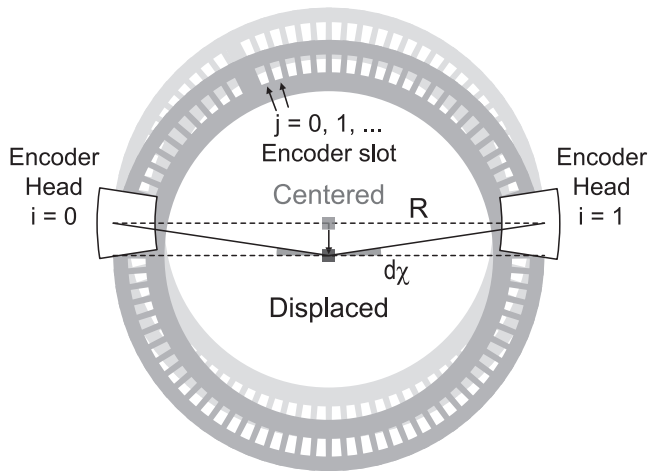

FIG. 20. Schematic diagram of the rotating CHWP on the scanning telescope. The gray area represents a telescope's receiver, while the light blue circle represents the rotor.

FIG. 22. Schematic diagram of the measurement setup of the off-center displacement. When the rotor is off-centered perpendicular to the line connecting the encoders, the pair incorrectly measures the rotation angle by $d\chi$. The off-center displacement can be calculated by Eq. (B3).

Sec. V F. The displacement perpendicular to the line connecting the pair of encoders is thus

$$\text{Displacement}_j = R \times \tan(d\chi_j), \qquad (B3)$$

where $R = 334$ mm is the radius of the encoder slots.

The measurement accuracy of the encoder angle shift due to off-center displacement is $0.02°$, which is negligible compared to the required accuracy of the polarization angle calibration. The SAT platform will rotate the boresight $\pm 60°$. Since the phase shift between the pair of encoders is at its maximum when the boresight angle is $0°$, the requirement of the accuracy of the polarization angle is satisfied at any boresight angle.

APPENDIX C: PRECAUTIONS

Successful operation of the CHWP requires paying careful attention to a number of system characteristics. This section presents a summary of the precautions we learned to take while building the CHWP and evaluating its performance.

Physical interference of the rotor is the most common inhibitor of CHWP rotation. This interference can be caused by misplaced or loose screws, nuts, tape, motor sprocket magnets, encoder or motor cables, or multi-layer insulation. To avoid the risk of physical interference, the use of nuts and tape is minimized, the screws are secured with a threadlocker (LOCTITE 263), and the motor sprocket magnets are secured with epoxy (Stycast 2850 FT). Moreover, the magnetic screws or mechanical parts, including 304 stainless steel, must not be used. This is because the rotor's magnet ring is strong enough to dislodge them and cause physical interferences.

Care must also be taken in the operation of electrical devices, including the encoders, motors, and grippers. Protective measures for electrical devices are crucial, such as the protection circuit for the optical encoders, the current limit function for the motor drive power source, and the limit switch for the grippers. Finally, drastic temperature changes must be avoided, while the encoder LEDs are biased, as exposure to rapidly changing environments can cause degradation.

REFERENCES

[1] M. Kamionkowski, A. Kosowsky, and A. Stebbins, "Statistics of cosmic microwave background polarization," Phys. Rev. D **55**, 7368–7388 (1997).

[2] M. Zaldarriaga and U. Seljak, "All-sky analysis of polarization in the microwave background," Phys. Rev. D **55**, 1830–1840 (1997).

[3] M. Kamionkowski, A. Kosowsky, and A. Stebbins, "A probe of primordial gravity waves and vorticity," Phys. Rev. Lett. **78**, 2058–2061 (1997).

[4] U. Seljak and M. Zaldarriaga, "Signature of gravity waves in the polarization of the microwave background," Phys. Rev. Lett. **78**, 2054–2057 (1997); arXiv:astro-ph/9609169.

[5] L. Abbott and S. Pi, *Inflationary Cosmology* (World Scientific Publishing Company, 1986).

[6] A. Linde, *Particle Physics and Inflationary Cosmology*, Contemporary Concepts in Physics series (CRC Press, 1990), Vol. 5, pp. 1–362; arXiv:hep-th/0503203 [hep-th].

[7] A. Linde, "Inflationary cosmology," in *Inflationary Cosmology* (Springer, Berlin, Heidelberg, 2007), pp. 1–54.

[8] U. Seljak and M. Zaldarriaga, "Direct signature of an evolving gravitational potential from the cosmic microwave background," Phys. Rev. D **60**, 043504 (1999).

[9] L. Page, G. Hinshaw, E. Komatsu et al., "Three-year *Wilkinson microwave anisotropy probe* (*WMAP*) observations: Polarization analysis," Astrophys. J., Suppl. Ser. **170**, 335 (2007); arXiv:astro-ph/0603450.

[10] Planck Collaboration, "Planck 2018 results. XI. Polarized dust foregrounds," Astron. Astrophys. **641**, A11 (2020).

[11] M. Zaldarriaga and U. Seljak, "Gravitational lensing effect on cosmic microwave background polarization," Phys. Rev. D **58**, 023003 (1998).

[12] L. Knox and Y.-S. Song, "Limit on the detectability of the energy scale of inflation," Phys. Rev. Lett. **89**, 011303 (2002).

[13] M. Kesden, A. Cooray, and M. Kamionkowski, "Separation of gravitational-wave and cosmic-shear contributions to cosmic microwave background polarization," Phys. Rev. Lett. **89**, 011304 (2002).

[14] U. Seljak and C. M. Hirata, "Gravitational lensing as a contaminant of the gravity wave signal in the CMB," Phys. Rev. D **69**, 043005 (2004).

[15] P. Ade, J. Aguirre, Z. Ahmed et al., "The Simons Observatory: Science goals and forecasts," J. Cosmol. Astropart. Phys. **2019**, 056; arXiv:1808.07445 [astro-ph.CO].

[16] M. H. Abitbol et al., "The Simons Observatory: Astro2020 Decadal Project Whitepaper," Bull. Am. Astron. Soc. **51**, 147 (2019); arXiv:1907.08284 [astro-ph.IM].

[17] A. Ali, S. Adachi, K. Arnold et al., "Small aperture telescopes for the Simons Observatory," J. Low Temp. Phys. **200**, 461–471 (2020).

[18] K. Kiuchi, S. Adachi, A. M. Ali et al., "Simons Observatory Small Aperture Telescope overview," Proc. SPIE **11445**, 114457L (2020); arXiv:2101.11917 [astro-ph.IM].

[19] N. Galitzki et al., "The Simons Observatory: Instrument overview," Proc. SPIE **10708**, 1070804 (2018); arXiv:1808.04493 [astro-ph.IM].

[20] N. Zhu, T. Bhandarkar, G. Coppi et al., "The Simons Observatory large aperture telescope receiver," Astrophys. J., Suppl. Ser. **256**, 23 (2021).

[21] S. C. Parshley, M. Niemack, R. Hills et al., "The optical design of the six-meter CCAT-prime and Simons Observatory telescopes," Proc. SPIE **10700**, 1070041 (2018); arXiv:1807.06678 [astro-ph.IM].

[22] S. W. Henderson et al., "Highly-multiplexed microwave SQUID readout using the SLAC microresonator radio frequency (SMuRF) electronics for future CMB and sub-millimeter surveys," Proc. SPIE **10708**, 1070819 (2018); arXiv:1809.03689 [astro-ph.IM].

[23] Y. Li, K. Arnold, Z. Atkins et al., "Assembly and integration process of the high-density detector array readout modules for the Simons Observatory," J. Low Temp. Phys. **199**, 985–993 (2020).

[24]H. McCarrick, E. Healy, Z. Ahmed *et al.*, "The Simons Observatory microwave SQUID multiplexing detector module design," Astrophys. J. **922**, 38 (2021).

[25]Simons Observatory Collaboration, "simonsobs/bolocalc-so-model version v3r7 baseline," https://github.com/simonsobs/bolocalc-so-model/.

[26]N. Jarosik, C. L. Bennett, M. Halpern *et al.*, "Design, implementation, and testing of the microwave anisotropy probe radiometers," Astrophys. J., Suppl. Ser. **145**, 413 (2003).

[27]C. W. O'Dell, B. G. Keating, A. de Oliveira-Costa *et al.*, "CMB polarization at large angular scales: Data analysis of the POLAR experiment," Phys. Rev. D **68**, 042002 (2003).

[28]E. M. Leitch, J. M. Kovac, N. W. Halverson *et al.*, "Degree angular scale interferometer 3 year cosmic microwave background polarization results," Astrophys. J. **624**, 10 (2005).

[29]D. Barkats, C. Bischoff, P. Farese *et al.*, "Cosmic microwave background polarimetry using correlation receivers with the PIQUE and CAPMAP experiments," Astrophys. J., Suppl. Ser. **159**, 1 (2005).

[30]M.-T. Chen, C.-T. Li, Y.-J. Hwang *et al.*, "AMiBA: Broadband heterodyne cosmic microwave background interferometry," Astrophys. J. **694**, 1664 (2009).

[31]M. Bersanelli, N. Mandolesi, R. C. Butler *et al.*, "*Planck* pre-launch status: Design and description of the low frequency instrument," Astron. Astrophys. **520**, A4 (2010).

[32]QUIET Collaboration *et al.*, "Second season QUIET observations: Measurements of the CMB polarization power spectrum at 95 GHz," Astrophys. J. **760**, 145 (2012); arXiv:1207.5034 [astro-ph.CO].

[33]S. Moyerman, E. Bierman, P. A. R. Ade *et al.*, "Scientific verification of Faraday rotation modulators: Detection of diffuse polarized galactic emission," Astrophys. J. **765**, 64 (2013).

[34]S. Bryan, P. Ade, M. Amiri *et al.*, "A cryogenic rotation stage with a large clear aperture for the half-wave plates in the spider instrument," Rev. Sci. Instrum. **87**, 014501 (2016).

[35]N. J. Miller, D. T. Chuss, T. A. Marriage *et al.*, "Recovery of large angular scale CMB polarization for instruments employing variable-delay polarization modulators," Astrophys. J. **818**, 151 (2016).

[36]K. Lee, J. Choi, R. T. Génova-Santos *et al.*, "GroundBIRD: A CMB polarization experiment with MKID arrays," J. Low Temp. Phys. **200**, 384–391 (2020).

[37]K. Harrington, R. Datta, K. Osumi *et al.*, "Two year cosmology large angular scale surveyor (CLASS) observations: Long timescale stability achieved with a front-end variable-delay polarization modulator at 40 GHz," Astrophys. J. **922**, 212 (2021).

[38]B. R. Johnson, J. Collins *et al.*, "MAXIPOL: Cosmic microwave background polarimetry using a rotating half-wave plate," Astrophys. J. **665**, 42 (2007).

[39]T. Matsumura, "A cosmic microwave background radiation polarimeter using superconducting magnetic bearings," Ph.D. thesis, University of Minnesota, 2006.

[40]J. Klein and EBEX Collaboration, "A cryogenic half-wave plate polarimeter using a superconducting magnetic bearing," Proc. SPIE **8150**, 815004 (2011).

[41]A. Kusaka, T. Essinger-Hileman *et al.*, "Modulation of cosmic microwave background polarization with a warm rapidly rotating half-wave plate on the Atacama B-Mode Search instrument," Rev. Sci. Instrum. **85**, 024501 (2014).

[42]C. A. Hill, S. Beckman, Y. Chinone *et al.*, "Design and development of an ambient-temperature continuously-rotating achromatic half-wave plate for CMB polarization modulation on the POLARBEAR-2 experiment," Proc. SPIE **9914**, 99142U (2016).

[43]B. R. Johnson, F. Columbro, D. Araujo *et al.*, "A large-diameter hollow-shaft cryogenic motor based on a superconducting magnetic bearing for millimeter-wave polarimetry," Rev. Sci. Instrum. **88**, 105102 (2017); arXiv:1706.05963 [astro-ph.IM].

[44]C. A. Hill, A. Kusaka, P. Ashton *et al.*, "A cryogenic continuously rotating half-wave plate mechanism for the POLARBEAR-2b cosmic microwave background receiver," Rev. Sci. Instrum. **91**, 124503 (2020).

[45]F. T. Matsuda, "Optics design development of the Simons Observatory Small Aperture Telescopes," Proc. SPIE **11445**, 114456Z (2020).

[46]S. Takakura, M. A. O. Aguilar-Faúndez, Y. Akiba *et al.*, "Measurements of tropospheric ice clouds with a ground-based CMB polarization experiment, POLARBEAR," Astrophys. J. **870**, 102 (2019); arXiv:1809.06556 [astro-ph.IM].

[47]M. A. Petroff, J. R. Eimer, K. Harrington *et al.*, "Two-year cosmology large angular scale surveyor (CLASS) observations: A first detection of atmospheric circular polarization at Q band," Astrophys. J. **889**, 120 (2020); arXiv:1911.01016 [astro-ph.IM].

[48]S. E. Church, "Predicting residual levels of atmospheric sky noise in ground-based observations of the cosmic background radiation," Mon. Not. R. Astron. Soc. **272**, 551–569 (1995).

[49]R. Dünner, M. Hasselfield, T. A. Marriage *et al.*, "The Atacama Cosmology Telescope: Data characterization and map making," Astrophys. J. **762**, 10 (2012); arXiv:1208.0050 [astro-ph.IM].

[50]J. Errard, P. Ade, Y. Akiba *et al.*, "Modeling atmospheric emission for CMB ground-based observations," Astrophys. J. **809**, 63 (2015).

[51]T. W. Morris, R. Bustos, E. Calabrese *et al.*, "The Atacama Cosmology Telescope: Modeling bulk atmospheric motion," Phys. Rev. D **105**, 042004 (2022); arXiv:2111.01319 [astro-ph.IM].

[52]Y. D. Takahashi, P. A. R. Ade, D. Barkats *et al.*, "Characterization of the BICEP telescope for high-precision cosmic microwave background polarimetry," ApJ **711**, 1141–1156 (2010); arXiv:0906.4069 [astro-ph.CO].

[53]D. S. Swetz, P. A. R. Ade, M. Amiri *et al.*, "Overview of the Atacama Cosmology Telescope: Receiver, instrumentation, and telescope systems," Astrophys. J., Suppl. Ser. **194**, 41 (2011).

[54]J. E. Austermann, K. A. Aird, J. A. Beall *et al.*, "SPTpol: An instrument for CMB polarization measurements with the South Pole Telescope," Proc. SPIE **8452**, 84521E (2012).

[55]M. Shimon, B. Keating, N. Ponthieu, and E. Hivon, "CMB polarization systematics due to beam asymmetry: Impact on inflationary science," Phys. Rev. D **77**, 083003 (2008); arXiv:0709.1513 [astro-ph].

[56]S. Pancharatnam, "Achromatic combinations of birefringent plates," Proc. Indian Acad. Sci. - Sec. A **41**, 137–144 (1955).

[57]EBEX Collaboration, "The EBEX balloon-borne experiment—Optics, receiver, and polarimetry," Astrophys. J., Suppl. Ser. **239**, 7 (2018).

[58]L. Moncelsi, P. A. R. Ade, F. E. Angilè *et al.*, "Empirical modelling of the BLAST-Pol achromatic half-wave plate for precision submillimetre polarimetry," Mon. Not. R. Astron. Soc. **437**, 2772–2789 (2013).

[59]Y. Sakurai, T. Matsumura, N. Katayama *et al.*, "Breadboard model of the polarization modulator unit based on a continuously rotating half-wave plate for the low-frequency telescope of the LiteBIRD space mission," Proc. SPIE **11453**, 114534E (2020).

[60]T. Essinger-Hileman, A. Kusaka *et al.*, "Systematic effects from an ambient-temperature, continuously rotating half-wave plate," Rev. Sci. Instrum. **87**, 094503 (2016).

[61]M. Monelli, E. Komatsu, A. E. Adler, M. Billi, P. Campeti, N. Dachlythra, A. J. Duivenvoorden, J. E. Gudmundsson, and M. Reinecke, "Impact of half-wave plate systematics on the measurement of cosmic birefringence from CMB polarization," J. Cosmol. Astropart. Phys. **2023**, 034.

[62]J. Sugiyama *et al.*, "The Simons Observatory: Development and optical evaluation of achromatic half-wave plates," J. Low Temp. Phys. (published online) (2024).

[63]Cryomech, PT-420s, https://www.cryomech.com/products/pt420/.

[64]S. Takakura, M. Aguilar, Y. Akiba, *et al.*, "Performance of a continuously rotating half-wave plate on the POLARBEAR telescope," J. Cosmol. Astropart. Phys. **2017**, 8.

[65]K. D. Crowley, P. Dow, J. E. Shroyer *et al.*, "The Simons Observatory: A large-diameter truss for a refracting telescope cooled to 1 K," Rev. Sci. Instrum. **93**, 055106 (2022).

[66]N. Galitzki *et al.*, "The Simons Observatory: Integration and testing of the first small aperture telescope, SAT-MF1" (unpublished).

[67]M. Salatino, J. Lashner, M. Gerbino, S. M. Simon, J. Didier *et al.*, "Studies of systematic uncertainties for Simons Observatory: Polarization modulator related effects," Proc. SPIE **10708**, 1070848 (2018); arXiv:1808.07442 [astro-ph.IM].

[68]POLARBEAR Collaboration, "Improved upper limit on degree-scale CMB B-mode polarization power from the 670 square-degree POLARBEAR survey," Astrophys. J. **931**, 101 (2022).

[69]See https://www.spira-emi.com/ for Spira Manufacturing Corporation.

[70]D. W. Wisander, L. P. Ludwig, and R. L. Johnson, "Wear and friction of various polymer laminates in liquid nitrogen and in liquid hydrogen," NASA Technical Note No. TN D-3706 (NASA, 1966).

[71]Y. Sakurai, P. Ashton, A. Kusaka et al., "Half-meter scale superconducting magnetic bearing for cosmic microwave background polarization experiments," J. Phys.: Conf. Ser. **1590**, 012060 (2020).

[72]Y. Sakurai, T. Matsumura, N. Katayama et al., "Design and development of a polarization modulator unit based on a continuous rotating half-wave plate for LiteBIRD," Proc. SPIE **10708**, 107080E (2018).

[73]Can Superconductors, CSYL-28, https://www.can-superconductors.com/.

[74]Shin-Etsu Chemical Co., Ltd., https://www.shinetsu.co.jp/en/.

[75]SMC Corporation LEY32C-30B-S11P1.

[76]See https://huntvac.com/ for Huntington Vacuum Products.

[77]K&J magnetics Inc., D11-N52, https://www.kjmagnetics.com/proddetail.asp?prod=D11-N52.

[78]Vishay, TEMD1020, https://www.vishay.com/docs/81564/temd1000.pdf.

[79]Vishay, VSMB294008G, https://www.vishay.com/docs/84228/vsmb294008rg.pdf.

[80]APW Electromagnet, FC-6035, https://apwcompany.com/fc-6035/.

[81]Omega, CNI16D54-EIT, https://www.jp.omega.com/pptst/CNI_SERIES.html.

[82]Lake Shore, Model 240, https://www.lakeshore.com/products/categories/overview/temperature-products/cryogenic-temperature-modules/240-series-input-modules.

[83]Lake Shore, HGT-3010, https://shop.lakeshore.com/default/transverse-hall-sensor-3010hgt-3010.html.

[84]Y. Sakurai, T. Matsumura, H. Kataza et al., "Estimation of the heat dissipation and the rotor temperature of superconducting magnetic bearing below 10 K," IEEE Transa. Appl. Supercond. **27**, 1–4 (2017).

[85]B. J. Koopman, J. Lashner, L. J. Saunders et al., "The Simons Observatory: Overview of data acquisition, control, monitoring, and computer infrastructure," Proc. SPIE **11452**, 1145208 (2020).

[86]Y. Inoue, T. Matsumura, M. Hazumi et al., "Cryogenic infrared filter made of alumina for use at millimeter wavelength," Appl. Opt. **53**, 1727 (2014).

[87]M. J. Persky, "Review of black surfaces for space-borne infrared systems," Rev. Sci. Instrum. **70**, 2193–2217 (1999).

[88]Kikusui Electronics Corporation, PMX35-3A.

[89]T. Tsan, N. Galitzki, A. M. Ali et al., "The effects of inclination on a two stage pulse tube cryocooler for use with a ground based observatory," Cryogenics **117**, 103323 (2021).

[90]Analog Devices, adxl345, https://www.analog.com/en/products/adxl345.html.

[91]P. Tiwari, X. D. Wu, S. R. Foltyn et al., "Study of high-quality epitaxial YBCO thin films grown directly on Y-cut LiNbO$_3$," J. Electron. Mater. **25**, 131–135 (1996).

[92]Y. Sakurai, T. Matsumura, N. Katayama et al., "Development of a cryogenic remote sensing thermometer for CMB polarization experiment," in *29th International Symposium on Space Terahertz Technology (ISSTT 2018)* (Curran Associates, 2018), pp. 169–174.

[93]The minimum elevation angle of the SAT platform is 20°.

[94]BeagleBone Black, Beagle Board, https://beagleboard.org/black.

[95]Range Commanders Council, "IRIG Standard 200-16: IRIG serial time code formats" (2016).

[96]Guizhou Haotian Optoelectronics Co., Ltd.

[97]K. N. Abazajian, P. Adshead, Z. Ahmed et al., "CMB-S4 Science Book, First Edition," arXiv:1610.02743 [astro-ph.CO] (2016).

[98]M. H. Abitbol, Z. Ahmed, D. Barron et al., "CMB-S4 Technology Book, First Edition," arXiv:1706.02464 [astro-ph.IM] (2017).

27 February 2024 19:16:45